We are IntechOpen, the world's leading publisher of Open Access books
Built by scientists, for scientists

6,900
Open access books available

186,000
International authors and editors

200M
Downloads

Our authors are among the

154
Countries delivered to

TOP 1%
most cited scientists

12.2%
Contributors from top 500 universities

CLARIVATE ANALYTICS
BOOK CITATION INDEX
INDEXED

WEB OF SCIENCE™

Selection of our books indexed in the Book Citation Index in Web of Science™ Core Collection (BKCI)

Interested in publishing with us?
Contact book.department@intechopen.com

Numbers displayed above are based on latest data collected.
For more information visit www.intechopen.com

Chapter 10

Mechanical Property Evaluation of Electrodeposited Nanocrystalline Metals by Micro-testing

Takashi Nagoshi, Tso-Fu Mark Chang and Masato Sone

Additional information is available at the end of the chapter

http://dx.doi.org/10.5772/61267

Abstract

Electrodeposition is a very important technology in the fabrication of micro-components for micro-electro-mechanical systems (MEMS) or integrated circuits. Evaluations of the materials used in these devices as 3D components should be conducted using micro-sized specimens due to the sample size effect on the practical use of the components. Nanocrystalline metals could be deposited using an electrodeposition method with supercritical CO_2 emulsion. Our experiment on the micro-specimens provides information on micro-mechanical testing of electrodeposited metals including the effect of sample size, grain size, and anisotropic structures on mechanical properties. In this chapter, recent studies on crystal growth in electrodeposition of metals and its evaluation using micron-sized testing will be presented.

Keywords: Electrodeposition, metal, texture, microstructure, strength, micro-testing

1. Introduction

1.1. Microstructure of electrodeposited metal

Micro-electro-mechanical systems (MEMS) devises are usually fabricated using film deposition process. Deposition of metallic film can be classified into two major categories, one is the dry process and the other is the wet process. Dry process involves the use of gas or metallic vapor for deposition or directly deposit metal atoms on the surface of a substrate by sputtering. The process is simple, but the deposition rate is very slow, such as sub-nm to several nm in a second [1, 2]. Thus, the deposition is limited to sub-μm-scale structures in industrial applications and not favorable for fabrication of MEMS components that require structural support.

INTECH
open science | open minds

© 2015 The Author(s). Licensee InTech. This chapter is distributed under the terms of the Creative Commons Attribution License (http://creativecommons.org/licenses/by/3.0), which permits unrestricted use, distribution, and reproduction in any medium, provided the original work is properly cited.

As one type of the wet process, electroplating has been used in the industrial fabrication of MEMS and integrated circuit (IC) thanks to the fast deposition rate, low production cost, and simple operation [3, 4].

In recent years, the miniaturization of MEMS and IC merges into a nano-scale regime, also called nanotechnology. The component size or wire width of the structures reach several tens of nanometers. In the filling of small gaps, some problems arise as schematically shown in Figure 1. Since liquid solutions are used in the wet process, when the substrate is not covered with the electrolyte or hydrogen gas, bubbles evolve in the reaction adsorbed on the substrate, the area not having contact with the electrolyte would lead to formation of voids and pin-holes [5]. To accomplish successful gap-filling, we have developed an electroplating method with supercritical CO_2 emulsion (EP-SCE) [6, 7]. In this system, micelles formed with surfactant encapsulates supercritical CO_2. These micelles randomly bounce on the surface of the cathode and desorb evolved hydrogen bubbles. In reaction areas where the micelle is in contact, deposition must be stopped and eventually resume with bulk concentration of electrolyte. These features, which are called periodic plating characteristics (PPC) [8, 9], will contribute to the gap or hole filling in EP-SCE and attained Cu filling of a hole 70 nm in diameter and 350 nm in depth as shown in Figure 2 [10, 11]. Results of the metal deposition using EP-SCE are summarized in Table 1. On each metal deposition, electrolytes with the same base were used while the EP-SCE contains additional surfactant and emulsified with supercritical CO_2.

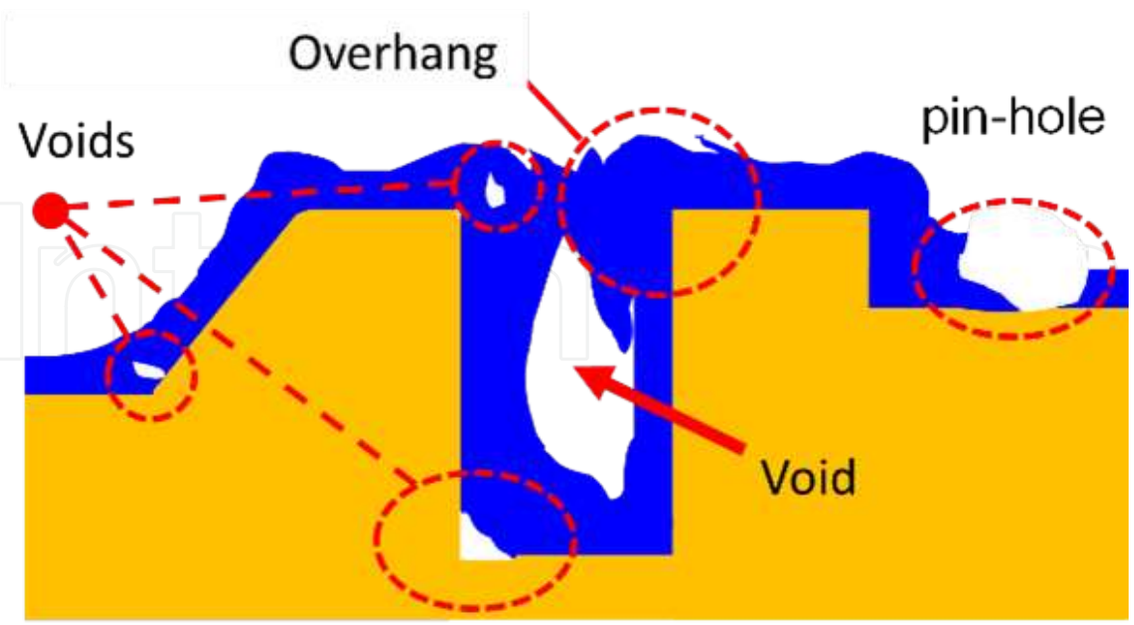

Figure 1. Failures found in filling of gaps with electrodeposition.

http://dx.doi.org/10.5772/61267

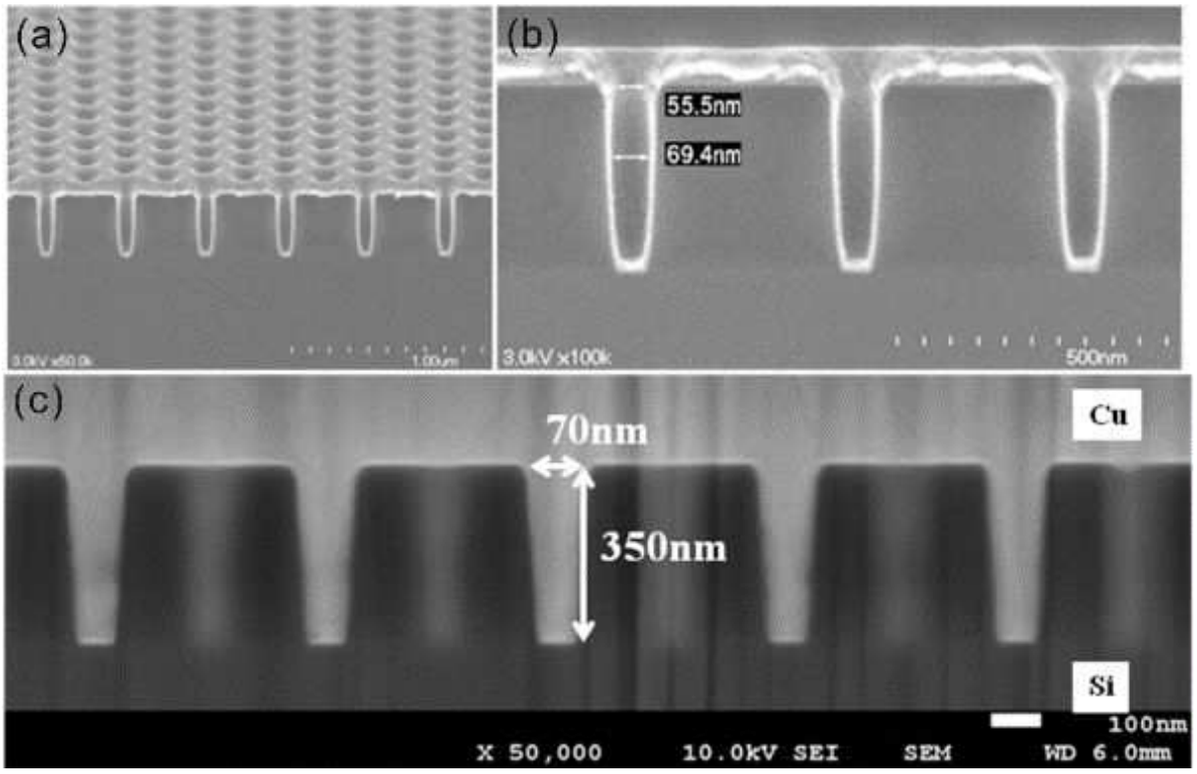

Figure 2. Cross-sectional SEM images of (a) Hole test element group (TEG) with holes of 70 nm in diameter and aspect ratio of 5, (b) expanded image of (a), and (c) TEG filled with Cu electroplated in EP-SCE with copper particles.

Plating method	Properties	Nickel [12, 13]	Copper [14]	Tin[15]
EP-SCE	Structures	Equi-axial grains	Equi-axial grains	Equi-axial grains
	Grain size	8 nm	100 nm	50 μm
	Impurities	2 at% of carbon	0.1 at% of carbon near substrate	Not detected by XPS
	Preferred orientation	No	-	-
CONV	Structures	Columnar grains	Polycrystalline with high density of twin boundary	Equi-axial grains
	Grain size	4.4x0.8 μm	1 μm	60 μm
	Impurities	Trace	0.1 at% of carbon near substrate	Oxygen as oxides
	Preferred orientation	<110> fiber texture	-	-

Table 1. Electrodeposited metals with EP-SCE and conventional (CONV) method

1.2. Mechanical property of electrodeposited metal

Micro-sized components used in MEMS fabricated by electrodeposition need to be tested to ensure device lifetime or tolerance to mechanical damage. MEMS are made up of components below 100 μm in size. For example, MEMS-based accelerometers or gyroscopes are widely used in cell phones, gaming consoles, and location-based devices. Some examples shown in Figure 3 are optical switch (3a) and gyro sensor (3b). Micro-components used in MEMS such as micro-spring, bending beams, and structural support of MEMS suffer from mechanical straining and need suitable mechanical properties. For mechanical property evaluation on such materials, conventional indentation or wear test is insufficient. Moreover, when the sample size comes to micro-scales, the classical physics are not always useful. Sample size effect, which will be described in a later section, emerges. Thus, a micro-testing method with a specimen whose sample size is in the same scales as the actual MEMS components is needed.

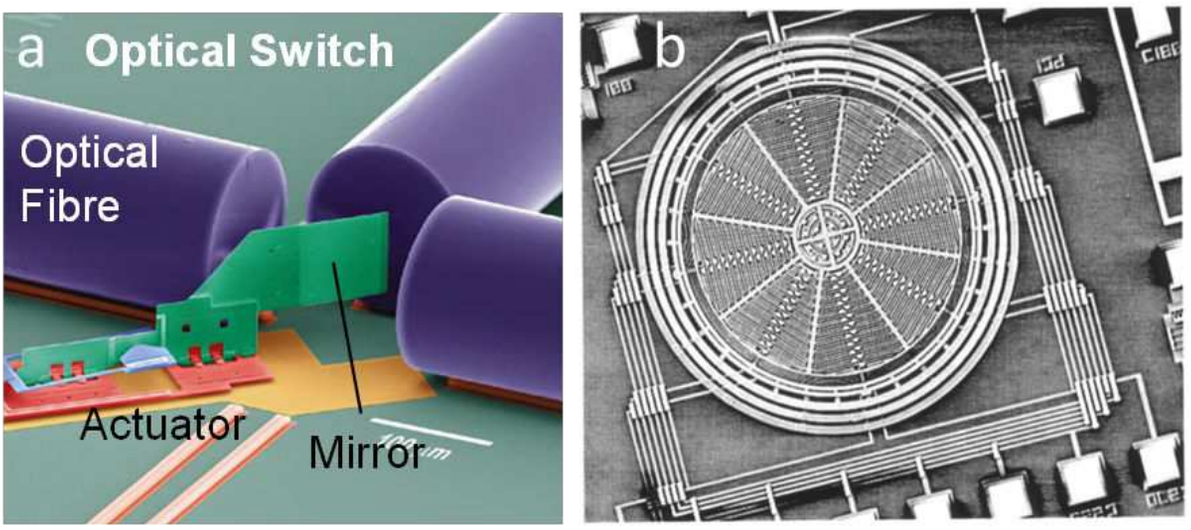

Figure 3. Examples of MEMS devises (a) optical switch and (b) gyro sensor.

1.3. Mechanical properties of small scale materials

The strength of metals has been shown to increase with decreasing sample size, known as "smaller is stronger" and also referred to as size effect [16]. For example, thin film experiments, including wafer curvature [17] bulge tests [18] and MEMS-based tests [19], have consistently shown an increase of strength with decreasing sample size. The majority of research investigating the size effect of metals by means of the micro-testing technique has focused on single crystalline metals [20, 21, 22, 23, 24, 25] and metallic grasses [26, 27, 28, 29]. Only limited data exists for metals with microstructures. Rinaldi et al. [30] and Jang and Greer [31] have investigated nickel nanocrystalline nano-pillars. However, their trends for strength as a function of sample size show opposite trend: Jang and Greer observe a "smaller is weaker" power-law dependence in nanocrystalline Ni; while Rinaldi et al. report very scattered results with slight strengthening with decreasing sample size for 30 nm-grained nanocrystalline Ni.

http://dx.doi.org/10.5772/61267

Thus, currently the experimental findings for sample size effect on nanocrystalline materials are inconclusive, and there is much uncertainty with respect to the deformation mechanism and combined effect of different size effects. Sample size effect on polycrystalline pillar has great interest in industries owing to miniaturization of MEMS devices reaching to its component scales at sub-micro or nano regime.

2. Electrodeposited Nickel

2.1. Ni film in conventional electrodeposition

2.1.1. Microstructural development of Ni film

Crystal growth in conventional Ni electrodeposition is investigated using additive-free Watt's bath. The substrate was films of pure Cu annealed at 673 K for 1 hour in vacuum. Ni layers with a thickness of about 25 μm were electrodeposited under agitation with magnetic stirring bar.

Microstructure of film cross-sections were evaluated by a scanning electron microscope (SEM) equipped with an electron backscatter diffraction pattern (EBSD) detector. The orientation map shown in Figure 4a was overlaid with a grain boundary map where Σ3 boundaries were colored yellow. The fraction of grain boundary was summarized in Figure 4b as low-angle grain boundaries (LAGB) with misorientation between 2° and 15°, high-angle grain boundaries (HAGB) with misorientation above 15°, and Σ3 boundaries. Fine columnar grains with diameter of around 100–200 nm have grown toward the film surface as shown in Figure 4a. Most of the grain boundaries dividing columnar grains are Σ3 boundaries, corresponding to twin boundaries, although the stacking fault energy of Ni is relatively high [32]. High density of twins, 42% among HAGB in this film, was also reported in various kinds of electrodeposited metals [33, 34, 35].

Transmission electron microscopy (TEM) observations in the vicinity of the interface between the electrodeposited Ni and Cu are shown in Figure 5 as bright field TEM image in 5a and schematic illustration corresponding to the TEM image in 5b [12]. In the epitaxial region, only about 100-nm thick contains high density of dislocations. Misfit strain of 2.5% due to the difference in the lattice constants of Cu (3.615 nm) and Ni (3.524 nm) arises between the electrodeposited Ni layer and Cu substrate. We consider that the observed dislocations were introduced to accommodate this misfit strain. Since the orientation of the epitaxial region is almost the same as that of the Cu substrate, an epitaxial region was formed to minimize the interfacial energy between the electrodeposited Ni layer and Cu substrate. The misfit strain, however, restricts the growth of the epitaxial region up to about 100 nm. Ahead of the epitaxial regions, columnar grains without an orientation relationship with respect to the Cu substrate form are shown in Figure 4. TEM image of the Ni film 1.4 μm away from interface is shown in Figure 6. The thickness of the twin is about 10 nm, which is substantially narrower than the twins observed in EBSD shown in Figure 6. From the TEM observation, these narrow twins with a thickness of about 10 nm were frequently observed while they cannot be detected in

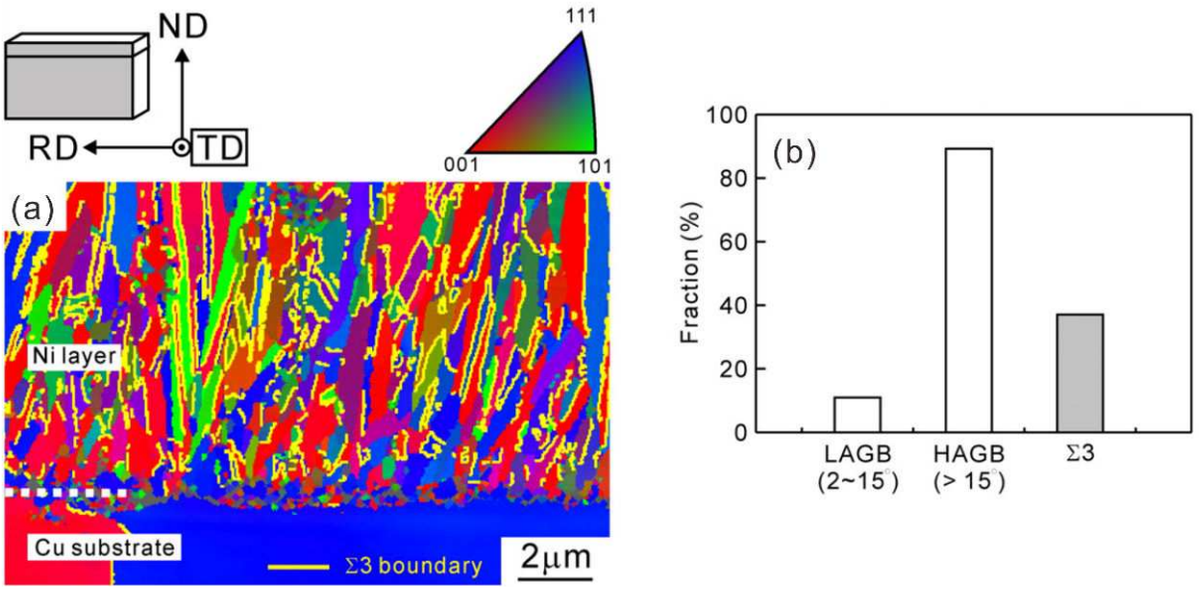

Figure 4. (a) Cross-sectional orientation maps of electrodeposited Ni layer. Σ3 boundaries are indicated as yellow lines in the figure. (b) Fractions of boundaries shown in (a) with different nature. Boundaries with misorientation between 2° and 15° classified as low-angle boundaries (LAGB) and misorientation angle above 15° are high-angle boundaries (HAGB). Σ3 boundaries that are HAGB satisfy the Brandon criterion (Σ3).

EBSD. We suppose that the twins in the electrodeposited Ni layer formed during electrodeposition reaction in the course of lateral movement of {111} facet shown in Figure 5a. Change in stacking sequence occurred at {111} facet could turn into a nucleus of twin grain. Fujiwara et al. [36, 37, 38] also proposed a similar model of twin formation parallel to the growth direction during the melt growth of Si.

2.1.2. Evaluation of anisotropic columnar grains in electrodeposited Ni by micron-sized cantilever

Mechanical properties of Ni film electrodeposited in conventional Watt's bath was evaluated using micro-cantilever. Cantilevers were milled out of the Ni film using focused ion beam (FIB) with different beam directions to investigate anisotropic mechanical properties. Micro-bending test had been used to investigate size dependent effect [39], local mechanical properties of lath martensite [40], and anisotropic fracture toughness of the NiAl single crystal [41]. In the cantilever specimen, deformation takes place at the fixed end on the tension at the upper side and compression at the lower side. Therefore, site specific influence of structure on the mechanical properties and deformation behavior can be examined.

Two cantilevers of 10 x 10 x 50 μm were fabricated with beams parallel and perpendicular to growth direction. As shown in Figure 7, columnar grains are aligned to the growth direction indicated in black arrow. The bending test had been carried out by indenting at the cross mark on the beam that is 40 μm away from fixed end. Force displacement curve in Figure 8 shows clear increase in the bending stress of the parallel cantilever. Maximum stress obtained was 2, 080 and 1, 582 MPa for the parallel and perpendicular cantilevers, respectively, with respect to the growth direction [42].

http://dx.doi.org/10.5772/61267

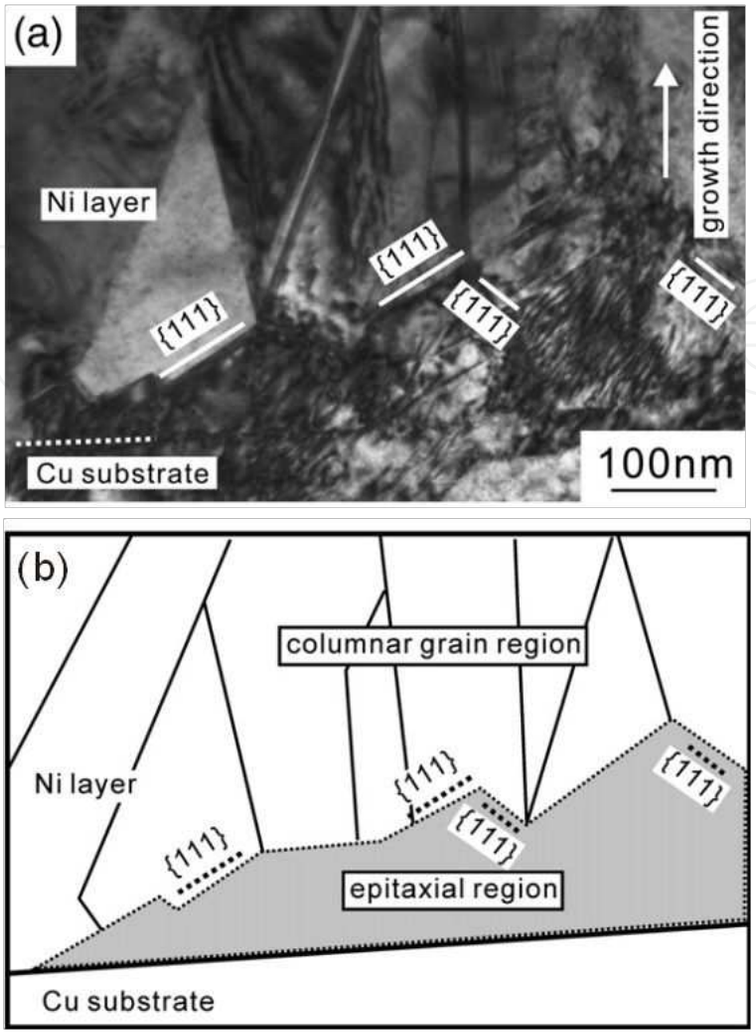

Figure 5. (a) Bright field TEM images showing the cross-sectional microstructure near the interface between the electrodeposited Ni layer and Cu substrate and (b) schematic illustration of (a).

In the deformation of fcc metals in which the slip system is {111} <110>, dislocation easily glides along the (111) twin plane. Ni film electrodeposited in conventional Watt's bath had high density of (111) coherent twin boundary parallel to growth direction. For the cantilever with parallel columnar grains, dislocations can move away from the stress concentration area. On the other hand, for the cantilever with perpendicular columnar grains, dislocations stop at the neutral plane. Longer slide distance of dislocations means effective stress relaxation at the fixed end, which enhances the apparent strength of the cantilever.

2.2. Ni film electrodeposited in supercritical CO_2 emulsified electrolyte

2.2.1. Nano-structured grains in Ni electrodeposited in supercritical CO_2 emulsified electrolyte

EP-SCE was conducted to deposit Ni on Cu substrate. Agitation with addition of surfactant, polyoxyethylene lauryl ether ($C_{12}H_{25}(OCH_2CH_2)15OH$) enables an electrolyte and supercritical

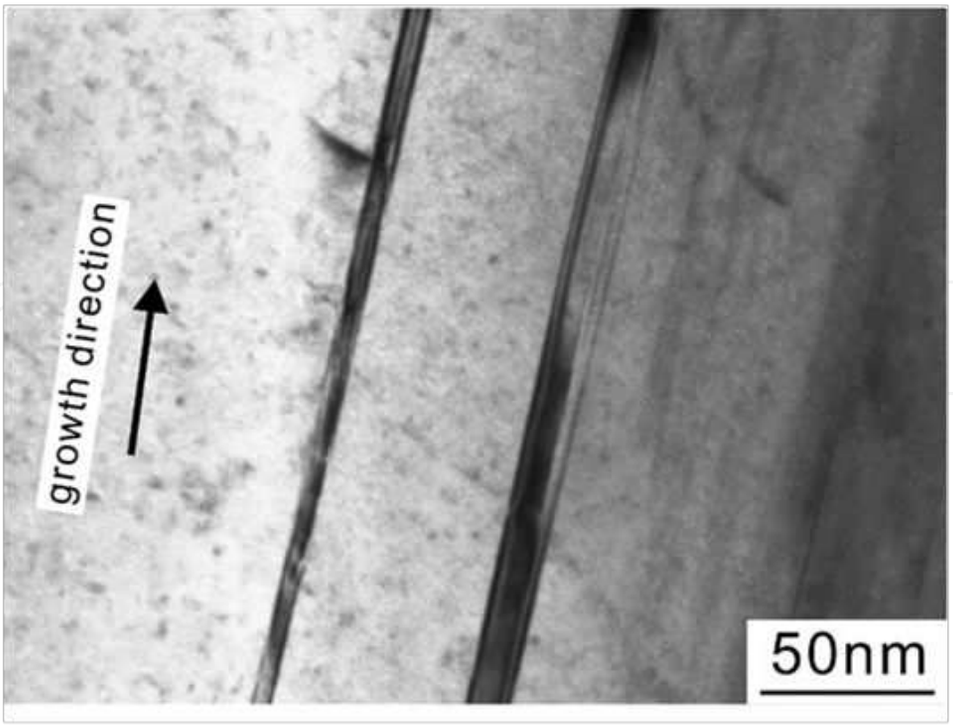

Figure 6. Bright field TEM image showing the microstructure within the columnar grain at 1.4 μm away from the interface between the electrodeposited Ni layer and Cu substrate.

CO_2 to form emulsions with CO_2-in-water (C/W) type micelles [43]. Additive-free Watt's bath was emulsified with CO_2. Electrodepositions on Cu substrate were conducted at different pressure of 6, 10, 15, 20 MPa including conventional electroplating (CONV).

The TEM bright field image shown inFigure 9is nickel film fabricated by EP-SCE at 15MPa viewed from growth direction [13]. Figure 10 shows average grain size of the films fabricated at different pressures based on measurement of around 100 grains in TEM. Equi-axial grains were found in all samples viewed from the sample surface and cross section. Grain refinement can be achieved by pulsed plating characteristics as stated by Chang et al., where the bouncing micelles promote nucleation by inhibiting grain growth [9]. Density of the CO_2 inside micelles increases with the increase in pressure, especially near the transition point from gas to supercritical phase. Change in density of the dispersed phase in emulsion will have an effect on the micelle structure and dispersion conditions. Thus, the change in grain size by different applied pressure was expected.

The impurity content of the film obtained from glow discharge optical emission spectroscopy (GDOES) should be noted. The carbon content could contribute to the grain refinement, which is shown in Table 2 including impurities of boron and oxygen. Comparing with CONV-plated nickel with and without surfactant, some impurities derived from surfactants were detected. However, in the emulsified state, surfactants consumed by the formation of micelles and the number of surfactants adsorbed and involved in the film could decrease. Similar concentration levels of oxygen among CONV- and EP-SCE-plated films imply surfactant extinction at the

http://dx.doi.org/10.5772/61267

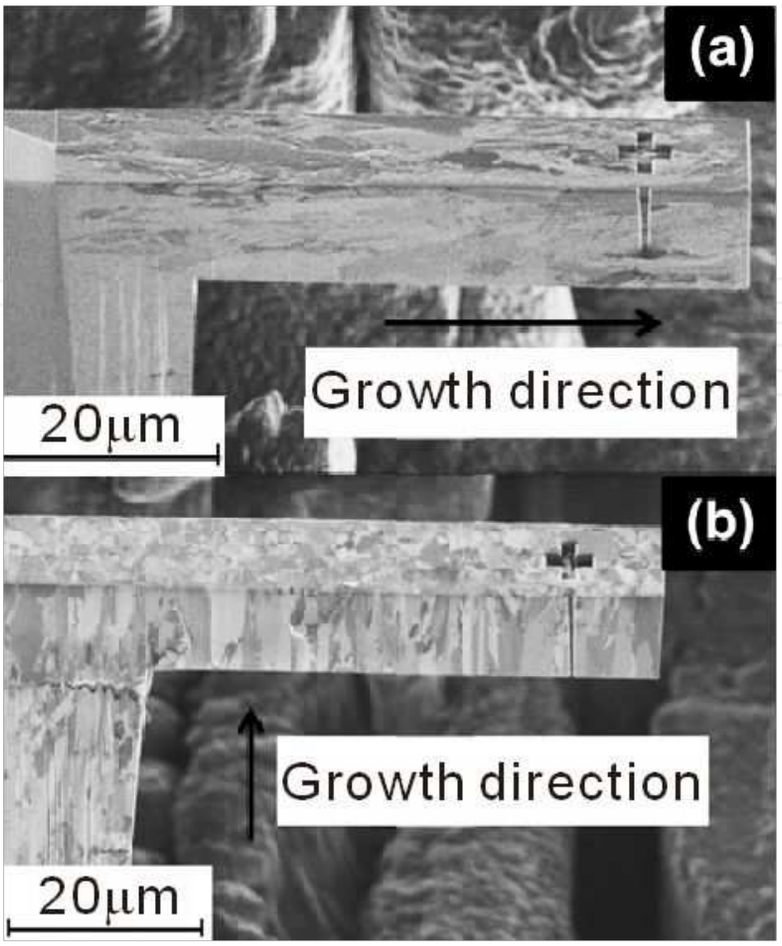

Figure 7. FIB images of the cantilevers fabricated by FIB. Beam directions are (a) 0° and (b) 90° with respect to growth direction indicated in black arrow.

surface when surfactants are mainly composed of carbon and oxygen. These results show that carbon derives from CO_2 dissolved in an electrolyte.

Deposited film	Concentration (at %)		
	Boron	Carbon	Oxygen
CONV without surfactant	0.000785	0.015	0.027
CONV with surfactant	0.00564	0.46	2.54
EP-SCE at 6MPa	0.000910	1.91	0.0220
EP-SCE at 10MPa	0.00114	2.43	0.0355
EP-SCE at 15MPa	0.00114	2.61	0.0305
EP-SCE at 20MPa	0.00102	2.17	0.0153

Table 2. Concentration of impurities in deposited film

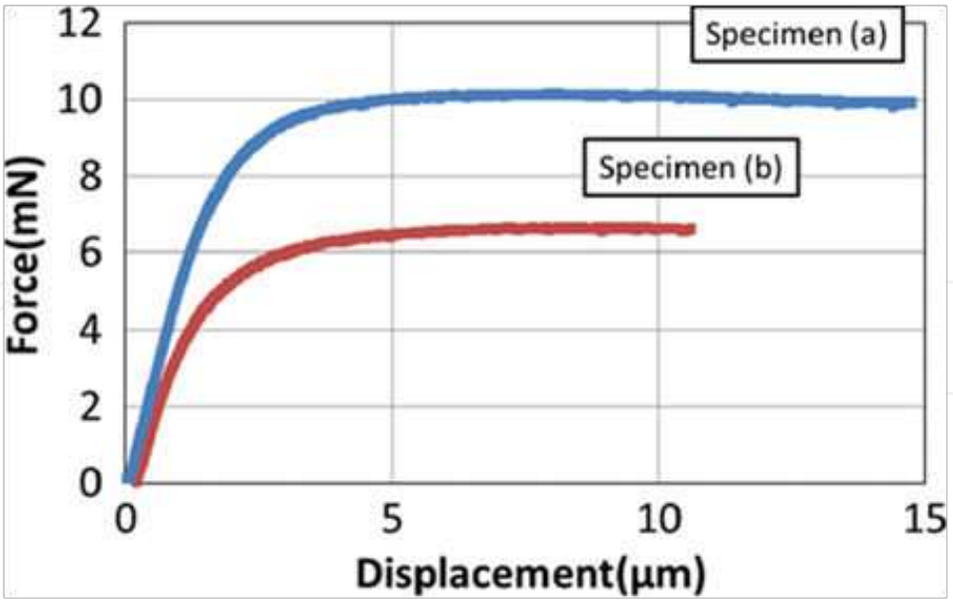

Figure 8. Load-displacement curve of the bending test. Specimen (a) and specimen (b) have beam directions of 0° and 90° with respect to growth direction, respectively.

Codeposition of carbon in electrodeposition has been reported by Chung and Tsai in supercritical CO_2 deposition [44] and Yamachika et al. using Au-Ni bath with citric acid [45], indicating that carbon originates from CO_2 and citric acid, respectively. Although carbon dioxide is chemically stable, production of hydrocarbons from carbon dioxide had been demonstrated in electrochemical reduction [46]. When the reduction of CO_2 dissolved in electrolyte occurred, carbon involved in the deposited nickel film results in Ni-C alloy deposition. In alloy electrodeposition where the foreign elements are incorporated as interstitials, crystalline size decreased when composition of foreign elements increased [47]. The alloying elements inhibit grain growth in the deposition process leading to the formation of amorphous film [48, 49]. The EP-SCE nickel also showed decreased grain size with increasing carbon content. Lattice constant observed in the X-ray diffraction (XRD) showed expansion corresponding to 2% of the solute carbon. Supersaturation of carbon solute in nickel deposits, where carbon can easily segregated on the grain boundary [50] and inhibit grain growth that results in nanocrystalline Ni deposits.

2.2.2. Mechanical property of nanocrystalline Ni evaluated by micro-compression test

Mechanical properties of nanocrystalline EP-SCE nickel, including the effect of grain size and sample size, were investigated using a micro-compression test. Non-tapered micro-pillars were fabricated by FIB from the region analyzed by the EBSD technique. Sequences of pillar fabrication are illustrated in Figure 11 with corresponding scanning ion microscope (SIM) images. In the course of fabrication, we first made a pillar that has the thickness of thin plate of around 100 μm and was shaped as shown in Figure 11a. Using irradiation of 45° from the thin plate, we made a small pillar from the bigger one as shown in Figure 11b. The ion beam from the side of the specimen allowed the fabrication of a pillar with uniform dimensions (non-

http://dx.doi.org/10.5772/61267

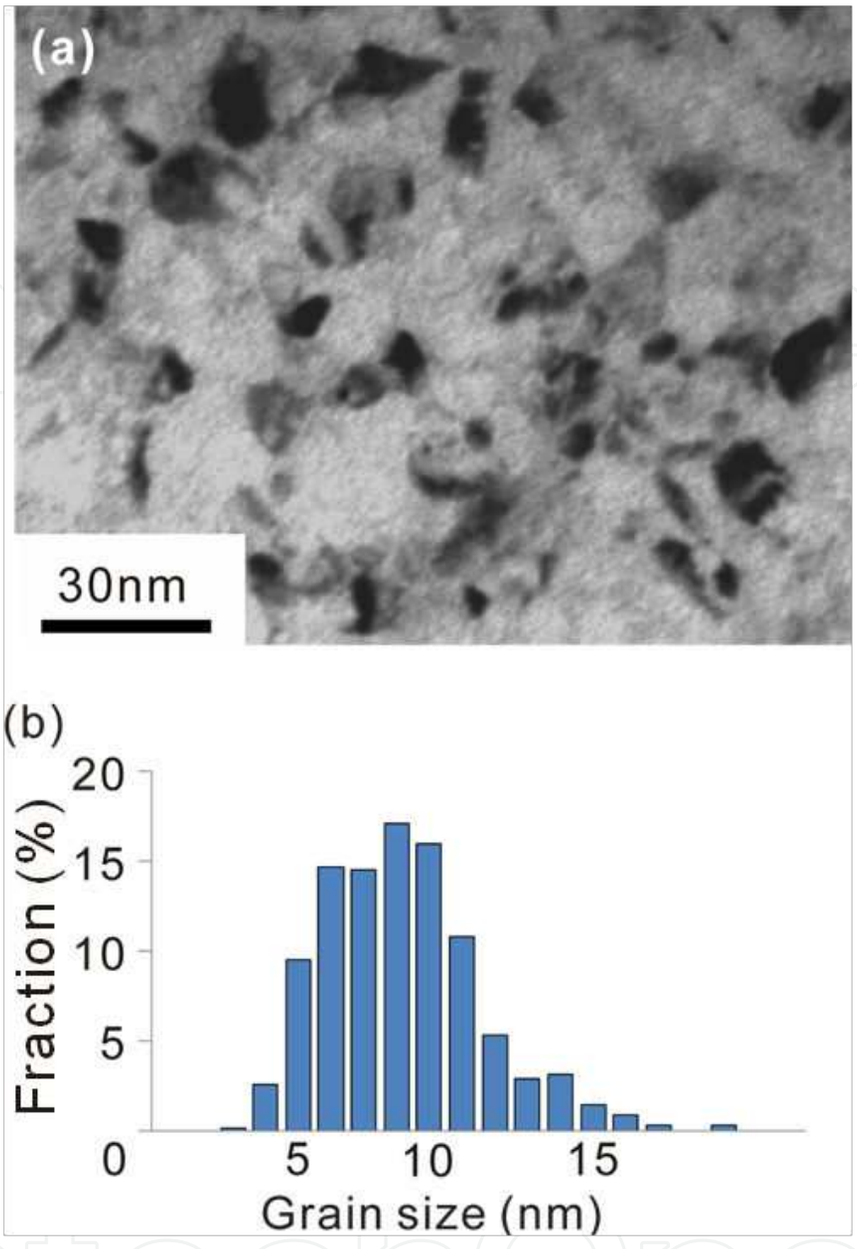

Figure 9. (a) Plan-view TEM bright field image of EP-SCE nickel and (b) grain size distribution from more than 500 of grains observed in TEM.

tapered, non-filleted). Finally, we milled each side of the pillar at a tilt angle of ±2.3° with 400 pA ion beam to minimize ion bombardment damage. A 20-μm square cross-section pillar fabricated from nickel film plated in EP-SCE at different pressures was employed to investigate grain size effect on plated nickel.

Micro-compression tests of nanocrystalline Ni with different grain size were conducted and the deformed pillars were observed as shown in Figure 12. All the pillars were deformed by broad shear banding crossing through top to bottom. However, the nickel film electrodeposited at 6 and 20 MPa, which has a larger grain size of 15 nm, had shown notable difference of

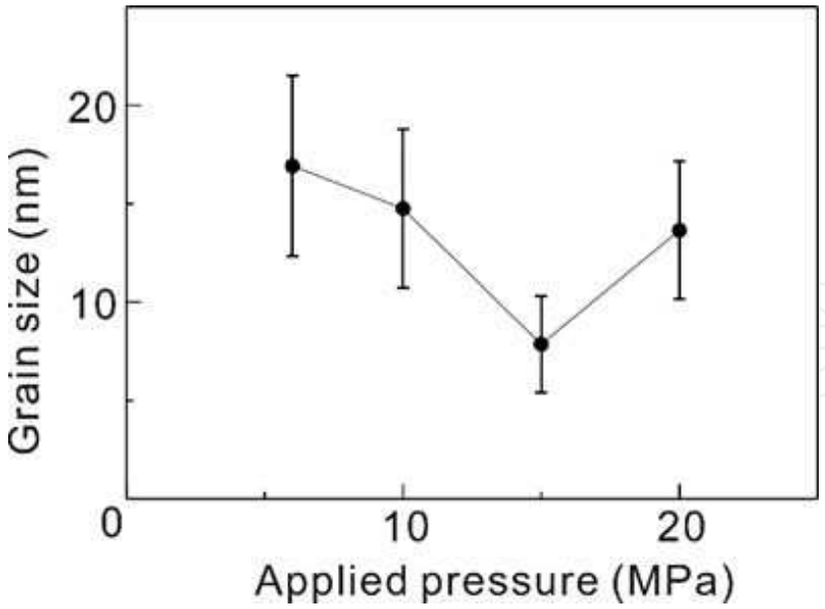

Figure 10. Grain size of the films electrodeposited at different pressures evaluated by TEM.

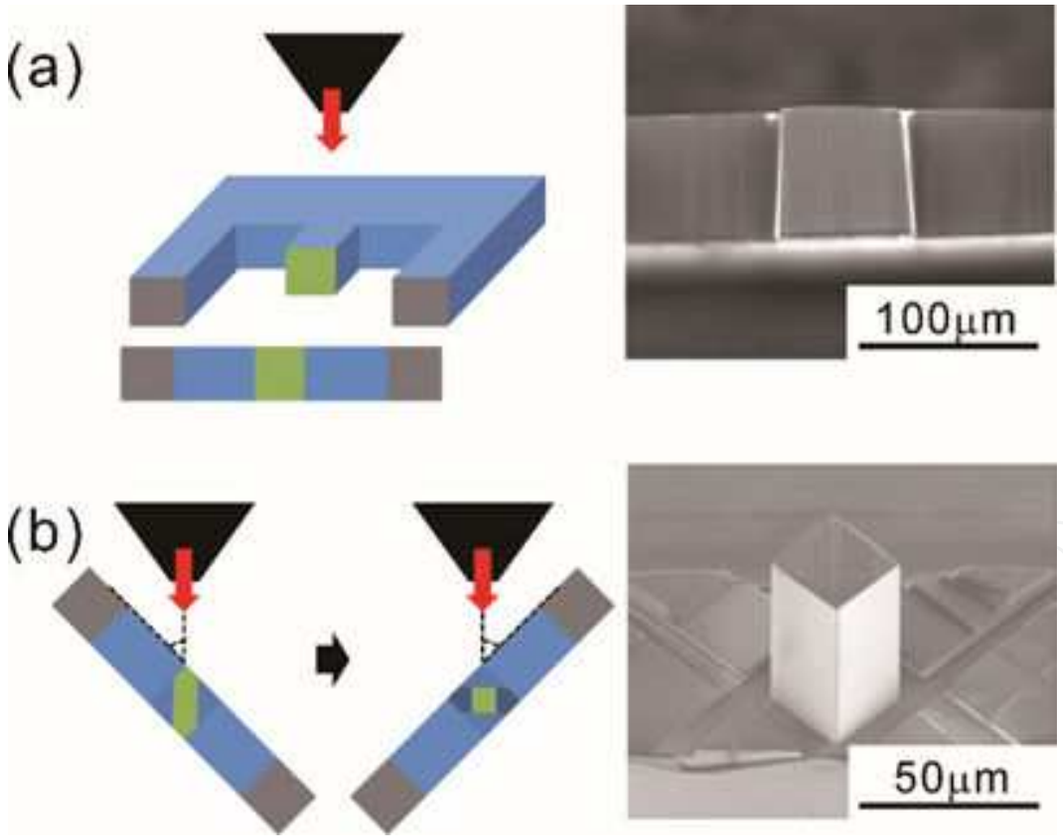

Figure 11. Procedures of making a compression pillar and SIM images showing the pillar after the procedure: (a) perpendicular irradiation and (b) irradiation from 45° from the thin plate.

bulging on the pillar surface as shown in Figure 12a and 12c. Micro-compression test results are shown in Figure 13 as true stress–true plastic strain curves. No clear relationships were found between deformation morphology and stress-strain behavior. Highest maximum stress of 3, 500 MPa was observed in the film electrodeposited at 15 MPa, which had the smallest grain size of 8 nm. The contribution on strengths of supersaturated carbon interstitials was calculated based on Fleischer formulation [51]. A 7.9 MPa of strengthening responsible for 2 at% of interstitial carbon is negligible compared to 3.5 GPa of maximum stress. The high strength in EP-SCE nickel could be due to a suppressed Hall-Petch breakdown. The strength of nanocrystalline Ni with grain size of 8 nm is on the extrapolated Hall-Petch slope from nickel alloy as shown in Figure 14. One-third of hardness values of pure nickel [52, 53, 54] and Ni-W alloy [55] are included in the Hall-Petch plot assuming Tabor relation [56] as well as 0.2% yield stress in the present micro-compression test. The suppression of Hall-Petch breakdown is consistent with a literature reported by Schuh et al., the hardness of Ni-W alloy has fallen at 8–9 nm and suggested that the alloying with tungsten has suppressed the Hall-Petch breakdown [55]. They concluded that the slow diffusion of tungsten in nickel increase required stress for activation of Coble creep and grain boundary sliding. Present electrodeposited nickel have 2.6 at% of carbon impurities and 2.0 at% of interstitial carbon, and the rest of the carbon could be segregated at the grain boundaries. Contrary to the tungsten in nickel, carbon has very high diffusivities in nickel via interstitial site diffusion. Yin et al. reported an effect of interstitials on creep deformation via Coble creep and grain boundary sliding [57]. On that literature, interstitially dissolved atoms are reported to effectively enhance creep resistance. Hall-Petch breakdown represents a transition of deformation mechanism from dislocation-mediated to grain-boundary-mediated. Thus, if the grain boundaries are reinforced by impurities, dislocation motion dominates the deformation at much smaller grain size and results in suppressed Hall-Petch breakdown [58].

Figure 15 displays the stress strain curves of pillars with sample size ranging from 5 μm to 30 μm prepared from single crystal and nanocrystalline Ni [59]. Due to multiple slip glides across the pillar or toward the base, large work hardening was observed in single crystal pillar compression. This result is similar to the compression of <111> oriented nickel pillar by Frick et al [20]. They observed dislocation lines throughout the pillar and base of the pillar, which indicates dislocation interaction by multiple slip and accumulation of dislocation at the pillar base. Thus, the stress needs to activate dislocation source inside the pillar increased with increasing strain. The following softening is believed to be a result of macroscopic shear by the activation of different slip systems due to increased stress. The deformation mechanism of nanocrystalline metal is believed to be a grain boundary process, such as grain boundary sliding or grain rotation. Considering the deformation mechanism, activation of dislocation source, which believed to be a possible explanation of size-dependent strength [16], did not play a main role in plastic deformation of nanocrystalline materials. Thus, the sample size effect on electrodeposited nanocrystalline Ni was not expected. However, the micro-compression test shows obvious increase in both yield stress and flow stress with decreasing sample size from 20 μm to 5 μm.

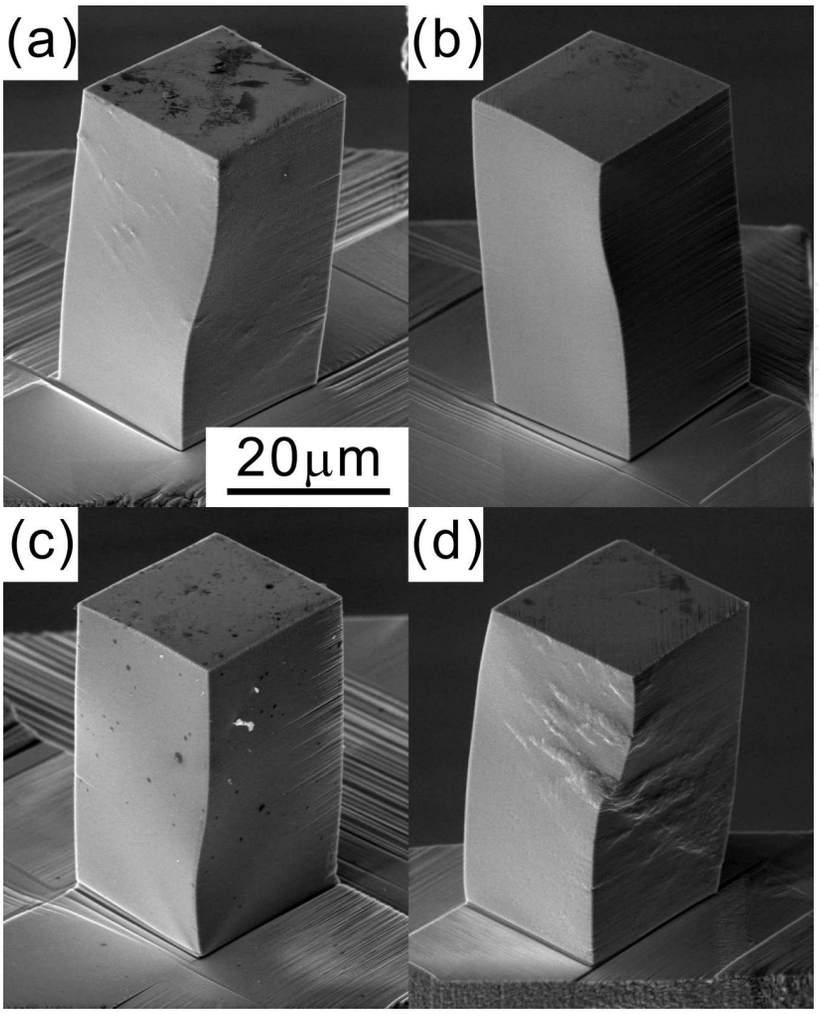

Figure 12. SEM images of the deformed pillars (a) 6 MPa, (b) 10 MPa, (c) 15 MPa, and (d) 20 MPa.

The stress as a function of pillar diameter for single crystal and nanocrystalline Ni was shown in Figure 16 [59]. The scaling exponent of 0.25 for the peak stress of single crystal Ni is small compared to 0.64 observed by Dimiduk et al. using non-tapered single crystal Ni (269) [21]. This can be explained by the change in dislocation mechanisms inside the pillars since different loading directions were taken. Relatively large sample sizes and multiple slips in the present work provide dislocation pile-ups and interaction of dislocation results in more dislocations inside the pillar that hinders sample size effect; note that the strength taken as a peak stress in stress strain curve is due to the uncertainty of yield point. For nanocrystalline Ni, which believed to deform without dislocation activation, the scaling exponent of 0.057 was observed. Although the exponent is quite low, strength obviously increased from 3.6 GPa to 4.1 GPa in 30 to 5 μm pillars. Reports on size effect of nanocrystalline materials are very limited and still controversial. Rinaldi et al. found increased strengths with the decreasing diameter of pillars from 270 to 160 nm in diameter-fabricated from nanocrystalline nickel with 30 nm of grain size [30]. On the contrary, Jang and Greer demonstrated size-induced weakening in 60 nm grained nickel nanopillars with a diameter between 3, 000 nm and 100 nm [31]. This contradiction can

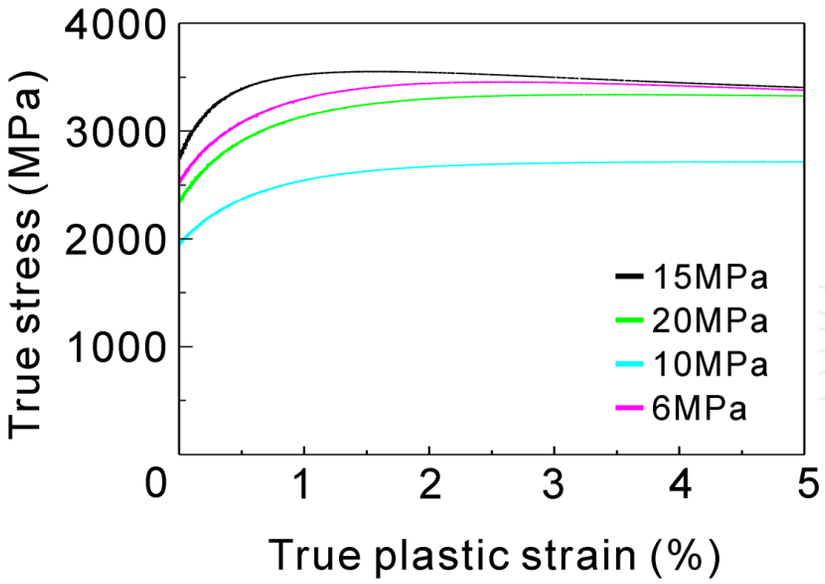

Figure 13. True stress–true plastic strain curves of a micro-pillar from films electrodeposited at different pressures.

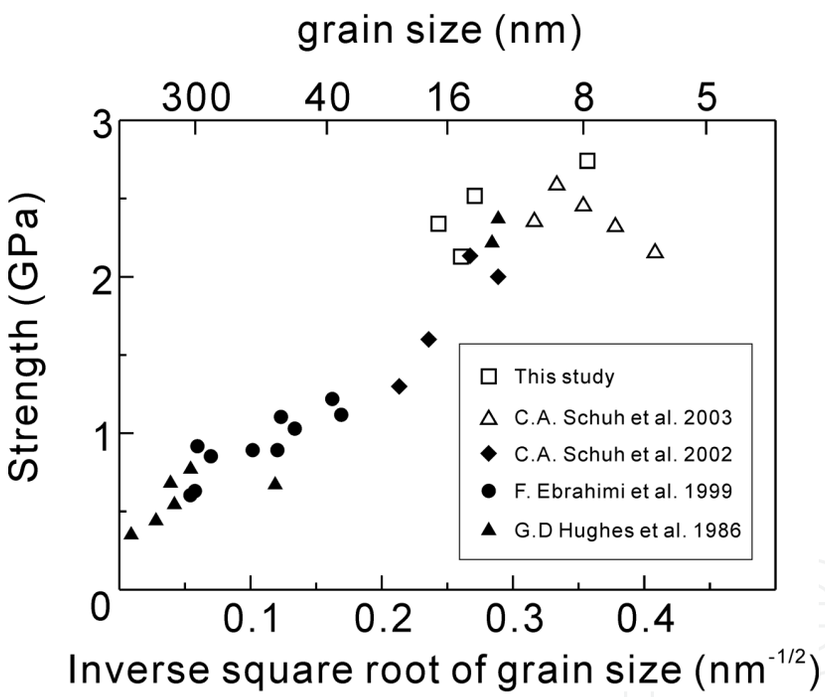

Figure 14. Hall-Petch plot representing 0.2% yield stress as well as one-third of hardness value found in literature.

be explained based on the deformation mechanisms. Jang observed a transition of deformation mechanisms from dislocation-mediated to grain-boundary-mediated, while grain-boundary-mediated deformation supposedly dominated in the present work. Grain boundary sliding is reported to involve several grains in formation of micro-shear band along the grain boundaries. Sums of these shear band formation will cause macroscopic yield in the present micro-compression test. Microscopic strains can generate on the large area of grain boundaries, which

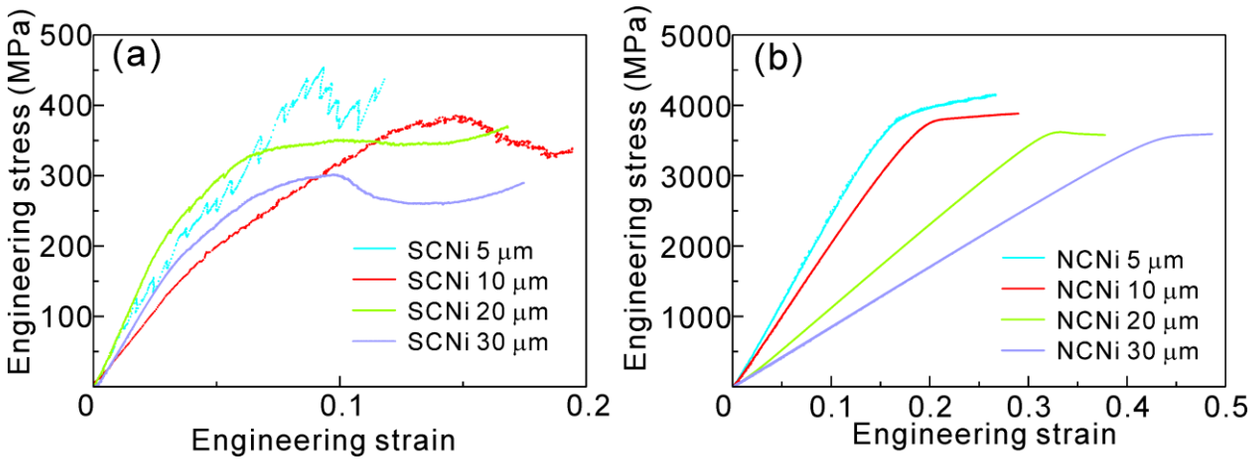

Figure 15. Engineering stress-strain curves for micro-compression of (a) single crystal Ni pillar and (b) nanocrystalline Ni pillars with different pillar sizes.

lies on the same plane with larger shear strain. This corrective motion of grain boundaries has been known as cooperative grain boundary sliding (CGBS) [60]. Zerin and Mukherjee observed bimodal distribution of sliding offset length on each CGBS event, which indicates breaking up of large sliding grain block into small grain blocks by secondary CGBS operation. This is observed with increase of strain, i.e., work hardening. CGBS events could initiate from the flat segment of grain boundaries and the number of these segments decreased when the sample size becomes smaller. Larger samples have segments of grain boundaries with longer distance to sliding direction and can deform with smaller stress. This is in good agreement with the change in exponent with increased strain, where large grain blocks in large samples can break up while small samples deform by CGBS with small grain blocks.

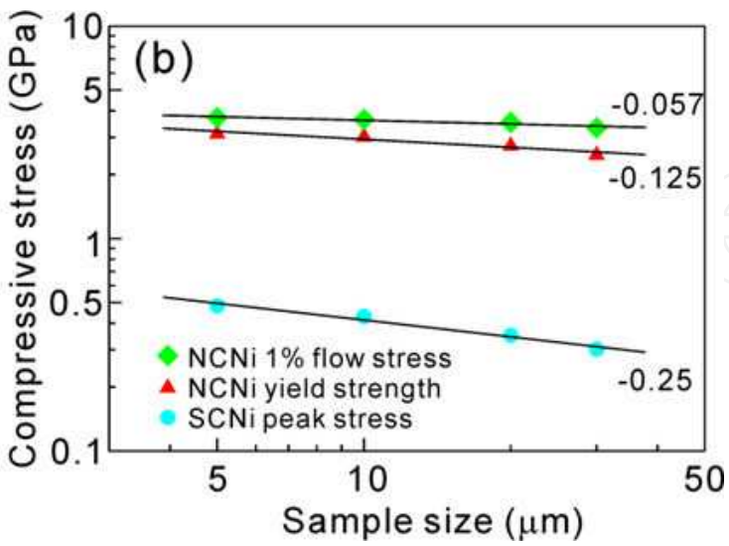

Figure 16. Strengths in micro-compression, peak stress for single crystal Ni, 1% flow stress, and 0.2% offset stress for nanocrystalline Ni are shown in a double-logarithmic graph. Solid lines represent power law fittings and each exponent is shown on the right.

http://dx.doi.org/10.5772/61267

3. Electrodeposited copper

3.1. Cu film electrodeposited in conventional electrolyte

3.1.1. Microstructure and self-annealing of Cu

Cu films were electrodeposited on Cu substrate in sulfate bath with and without additives. Current density of 2A/dm^2 and 10 A/dm^2 were used to deposit around 20 μm of Cu film. Investigation on microstructure of the electrodeposited Cu film was conducted immediately after the electroplating process and continued until self-annealing was observed. Cross-section EBSD was employed to measure grain size.

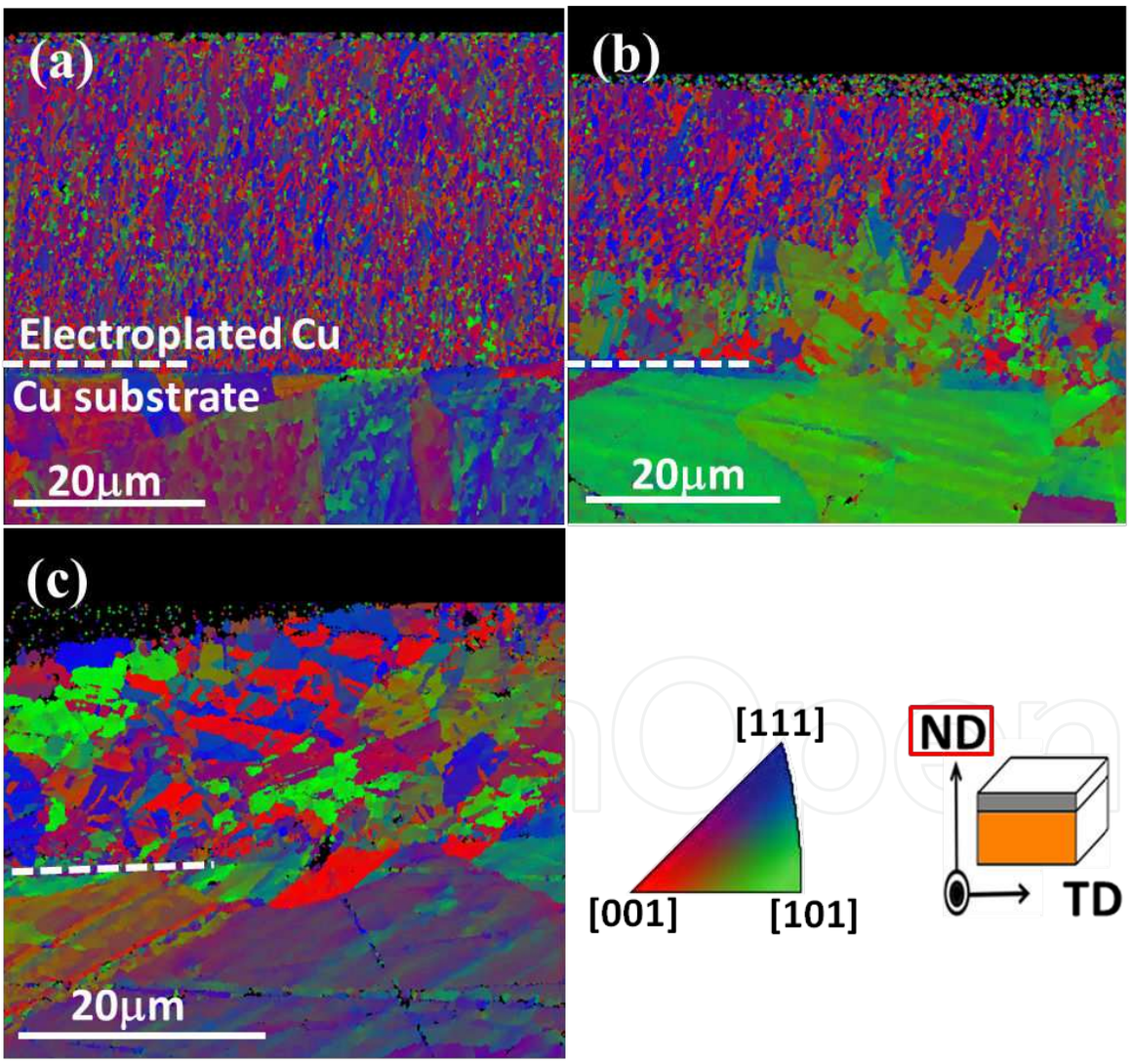

Figure 17. Cross-sectional EBSD maps for sample normal direction of self-annealed plated Cu films on Cu substrate at current density 100 mA/cm^2 (a) after 24 hours of incubation, (b) after 140 days of incubation, and (c) after 250 days of incubation. Dashed line indicates the interface.

Cross-sectional orientation maps obtained from EBSD analysis on Cu film deposited without additives are shown in Figure 17 [35]. Initial grain size was measured as 330 nm and enlarged to 860 nm after 250 days of incubation in vacuum. On the other hand, Cu film deposited with additives had large grain size near 1μm, which is obviously different from one of the Cu film that was as-deposited without additives and more similar to the film after self-annealing. The Cu film electrodeposited with additives may had been self-annealed soon after electrodeposition before characterization of structures. Many factors influence self-annealing, such as film thickness, incorporated impurities, and initial crystal structures [61, 62, 63]. Additives are usually used to smoothen the film and are known to refine initial grains while inhibiting grain growth during electroplating. Although the incorporated impurity inhibits recrystallization and slow down self-annealing, the significantly decreased grain size accelerates it and may have results in self-annealing within sample preparation for structure observation. Stangl et al. reported the effect of additives where the addition of a slight amount of additives cause nearly 8 times faster recrystallization at room temperature [61].

Table 3 shows the change in the fraction of grain boundaries with incubation time. All self-annealed microstructures in the electroplated Cu film contained a relatively high fraction of HAGB. Fraction of HAGB in the electroplated Cu film gradually decreased with the increase in incubation time. The increase in grain size results in decreased grain boundary area of HAGB, with lower boundary free energy in the materials. Therefore, the driving force of self-annealing of the electroplated Cu film at room temperature is boundary free energy of the high fraction of HAGB. This suggestion about driving force is supported by many researchers [62, 64]. In addition, the fraction of twin boundaries is increased by incubation time as shown in Table 3. Figure 18 shows the recrystallized area of Cu film after 140 days of incubation. Orientation of the individual grains are shown in Figure 18b as {110} pole figure with (111) plane, the sharing in each grain are marked with the dashed line. Grain A–E sharing (111) plane with each other, such as A/B, B/D, D/E, and B/C. Moreover, geometries of the twin plane and (111) plane seem identical, i.e., angles of grain boundaries between A and B, and D and E are close to the angles of (111) plane in the pole figure, which indicates these twin planes are coherent twin boundaries. The twin boundary, especially the coherent twin boundary has extremely low boundary free energy compared to HAGBs [64]. Practically, the fraction of HAGBs was found to decrease as self-annealing proceeds. Therefore, we suggest that the self-annealing was affected by the high fraction of HAGBs in the initial structure of the electroplated Cu film.

Incubation time	Fraction (%)		
	LAGB	HAGB	∑3 (twin)
24 hours	9.60	90.40	25.52
140 days	17.18	82.82	29.68
250 days	37.46	62.54	29.22

Table 3. Fractions of grain boundaries

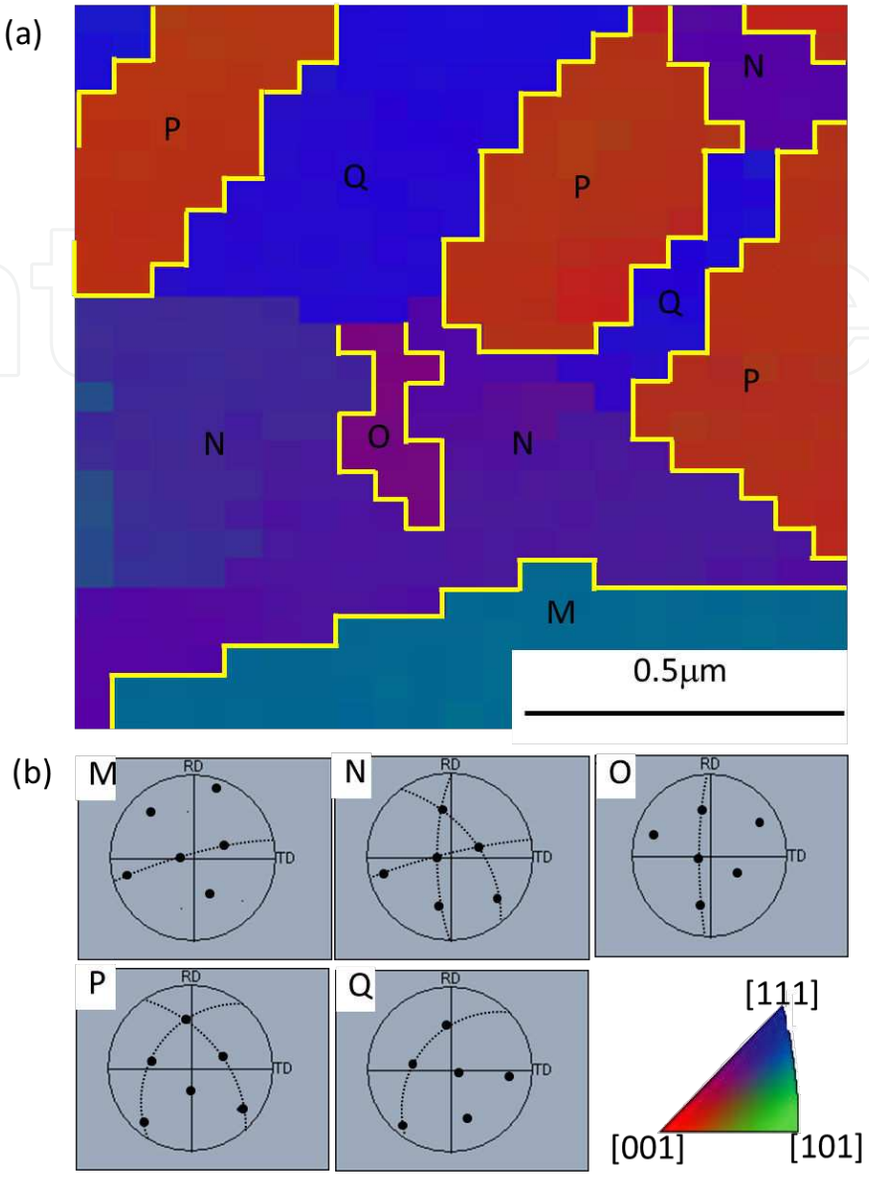

Figure 18. (a) Enlarged view of the cross-sectional EBSD map of plated Cu film after 140 days of incubation, and A to E in the map are equal to each grains. The yellow line shows twin boundaries. (b) {110} pole figures corresponding to the grain of A to E and the dashed line indicates the (111) plane.

3.1.2. Mechanical property of Cu electrodeposited in conventional electrolyte

The non-tapered micro-pillar was fabricated to evaluate mechanical properties and size effects of electrodeposited Cu films. The reduction in the number of grains within the sample may alter the mechanical properties of materials, which is one of the size effects [65]. In order to discuss the size effect, Cu films were electrodeposited using various current densities to change grain size whereas the size of all pillars is constant.

Table 4 shows average grain size, where measurement and calculation were made from more than 500 of grains observed in EBSD [66]. Grain boundary maps obtained from EBSD are shown

in Figure 19. Grain size of the electrodeposited Cu film was smaller when higher current density was used. Square pillars with 20 μm on a side were fabricated using FIB from each deposited film. Compression test results are shown in Figure 20. The strength of the pillar increased with decreasing grain size corresponding to the well-known Hall-Petch relationship [67, 68]. Slight difference in flow stress in the compression test of two pillars plated at 0.5 A/dm^2 might be caused by the specimen size effect stated by Armstrong [69]. When the ratio between the specimen size (S) and average grain size (G), shown as:

$$\frac{S}{G} = \frac{\text{Specimen Size}}{\text{Grain Size}}$$

is small, deformations of the specimen depends on the individual grain in the sample. In extreme conditions, for a single crystal specimen where S/G ratio below one, yield stress is determined by the orientation of the single crystal. When the number of grains within the specimen becomes lower, it means smaller S/G ratio; the effect of orientation for each grain in deformation behavior become stronger. The S/G ratio of pillars of 0.5 A/dm^2 is smaller than pillars of 5.0 A/dm^2 or 2.0 A/dm^2 as shown in Table 4. Therefore, the deviation of flow curve in the compression test with the pillars with S/G ratio is smaller than 25 affected crystallographic orientations.

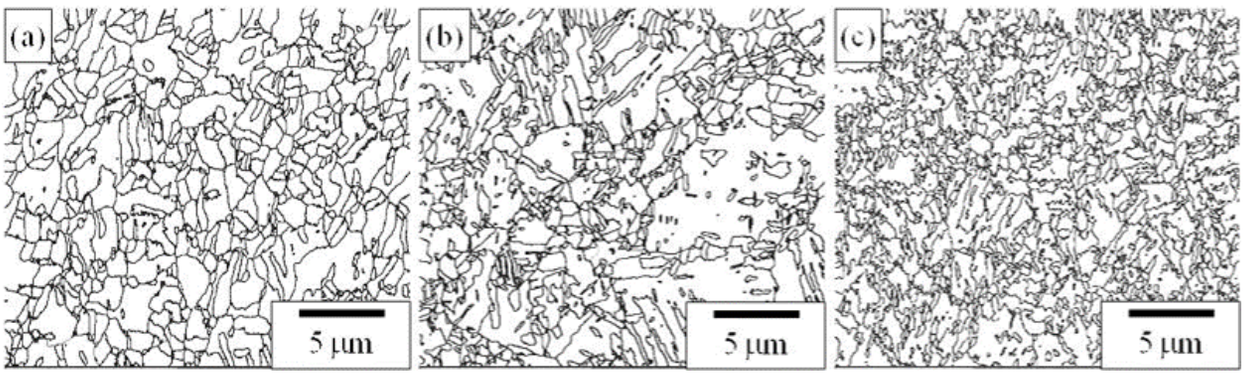

Figure 19. Grain boundary maps of electrodeposited Cu films. Cu film electrodeposited (a) at 0.5 A/dm^2, (b) at 2.0 A/dm^2, and (c) at 5.0 A/dm^2.

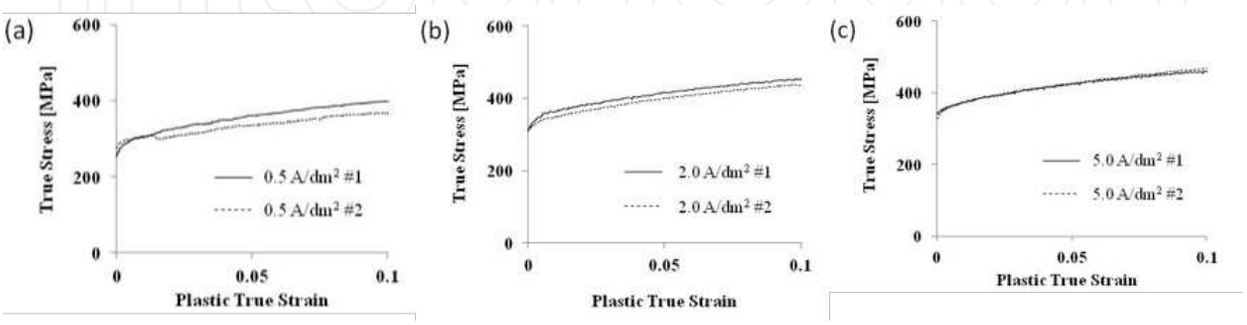

Figure 20. True stress–true plastic strain curves of the Cu pillars electrodeposited. Cu electrodeposited (a) at 0.5 A/dm^2, (b) at 2.0 A/dm^2, and (c): at 5.0 A/dm^2.

Current density [A/dm^2]	Grain Size [μm]	S/G ratio	Yield strength (0.2% offset) [MPa]
0.5	0.93	21.5	276
2.0	0.78	25.6	309
5.0	0.64	31.3	330

Table 4. Grain size, S/G ratio, and yield strength of the Cu pillars

3.2. Cu electrodeposited in supercritical CO_2 emulsified electrolyte

3.2.1. Nanostructure of electrodeposited Cu

Cu electrodeposition using EP-SCE with Watt's bath was conducted. Same high pressure apparatus in Ni deposition was used to deposit 10 μm of Cu film on Cu substrate. Figure 21 shows FIB images of deposited film [14]. Grain size of as-deposited Cu was significantly refined to 100 nm compared to CONV Cu. The cause of grain refinement could be corresponded to the one observed in Ni deposition. However, elemental analysis reveals very low level of impurities incorporated in the Cu film. Carbon impurity inside Cu film deposited in EP-SCE and CONV observed in GDOES is shown in Figure 22. Similar carbon distribution observed in CONV and EP-SCE Cu film indicates that the carbon impurity derives from an identical source. In both electrolytes, additives such as suppresser, accelerator, and leveler were used. These additives are adsorbed at the substrate and involved into the film during electroplating reaction. Thus, the CO_2 dissolved in the electrolyte used in EP-SCE had not reduced to carbon, which is different from Ni electrodeposition. More importantly, EP-SCE Cu showed significant microstructure evolution at room temperature as shown in Figure 21. Grain size of the film increased to 1 μm after two months of storage in a vacuum at room temperature. This is correspondent with self-annealing observed in Cu film deposited in conventional electroplating. Orientation maps shown in Figure 23 overlaid with HAGB and twin boundary in black and yellow lines. Structure change accompanied with the evolution of twin boundary was correspondingly observed with the one in the CONV Cu. High fraction of twin boundary, 70% of HAGB, should be the result of lowering boundary free energy in the process of self-annealing as discussed in Chapter 3.1.1.

3.2.2. Mechanical properties of nano-crystalline Cu electrodeposited in supercritical CO_2 emulsified electrolyte by micron-sized pillar

Mechanical properties of Cu before and after self-annealing was evaluated using micron-sized pillar fabricated using FIB. Figure 24 shows true stress-strain curve of Cu pillars fabricated from the films of as-deposited and two months after EP-SCE, including the results of CONV Cu [14]. A significant difference is observed in the mechanical strength among as-deposited EP-SCE and CONV. Engineering stress of the as-deposited EP-SCE pillar was about 300 MPa higher than the CONV pillar. And strength decreased by self-annealing to the same level of the CONV pillar. Deformation behavior is very similar in both self-annealed EP-SCE pillar and CONV pillar, in agreement to the identical microstructure observed. There is linear work hardening regime in the compression test of the CONV pillar and self-annealed EP-SCE pillar,

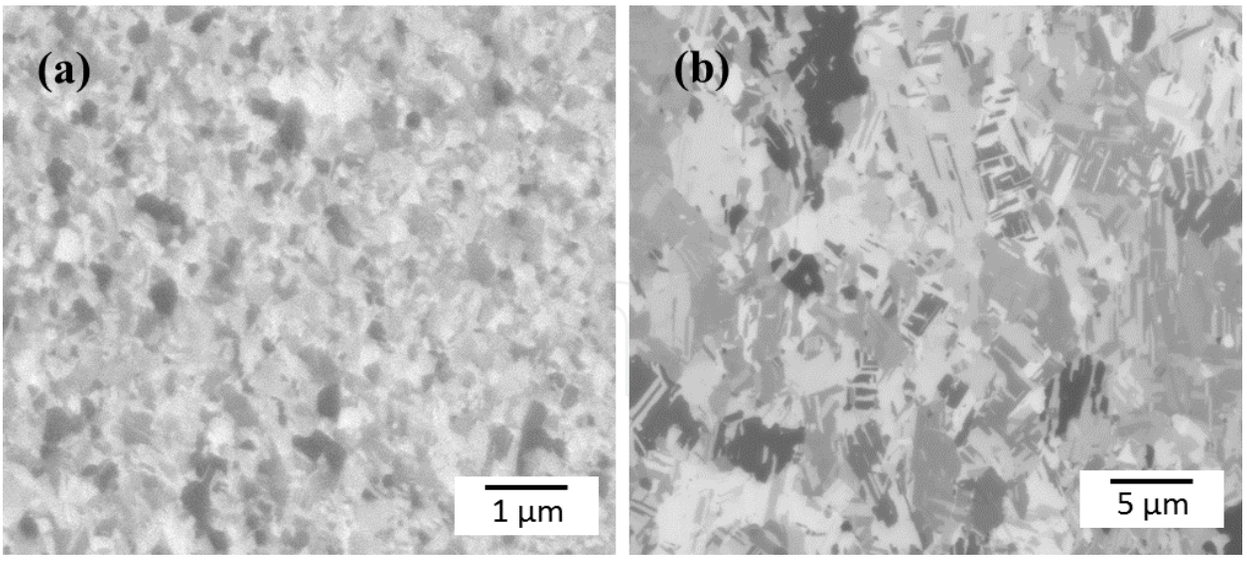

Figure 21. FIB images of Cu film obtained by EP-SCE (2.0 A/dm^2 for 120 min) (a) as electroplating (b) after two months.

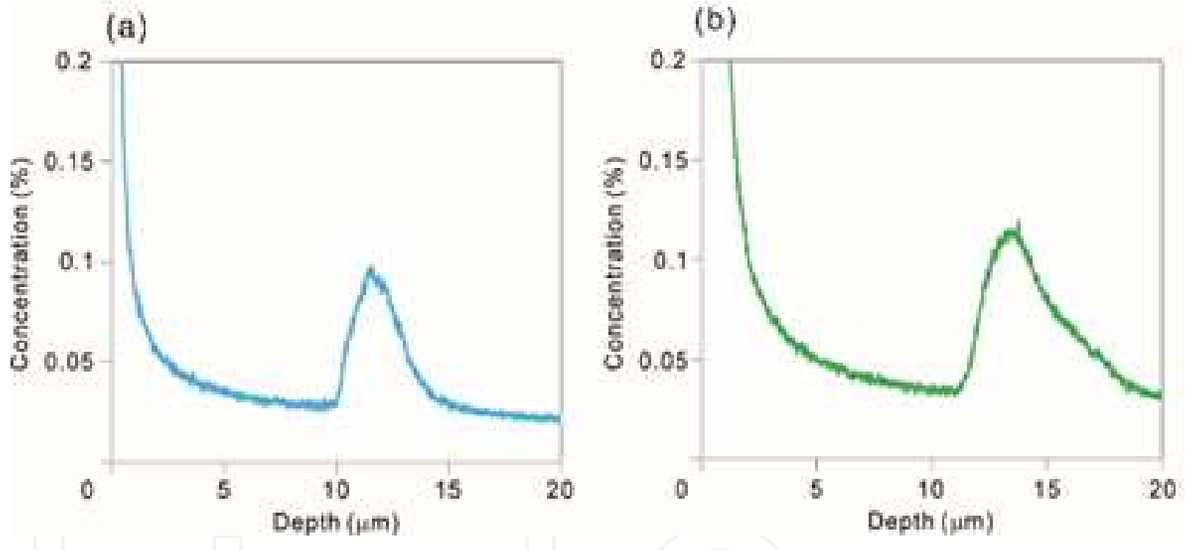

Figure 22. Carbon impurity concentrations in the copper film fabricated by (a) EP-SCE and (b) CONV observed using GDOES.

but is not observed in the compression test of as-deposited EP-SCE pillar. Figure 25 shows the SEM image of pillars after the compressive deformation. In the Cu pillar of CONV, many slip traces can be observed on the surface of the individual grains. Therefore, the deformations can be assumed to occur as dislocation activation inside grains. On the contrary, sharp shear band crossing through the pillar is observed in the as-deposited EP-SCE pillar, which explains no linear hardening in compressive deformation. SEM images from different sides indicated the shear sliding of the pillar top. Decrease in the cross-sectional area is followed by shear localization responsible for the work softening behavior in micro-compression of as-deposited EP-SCE. This is because the dislocation storage is strikingly limited by grain refinement when the grain size is in sub-micron meter regime.

http://dx.doi.org/10.5772/61267

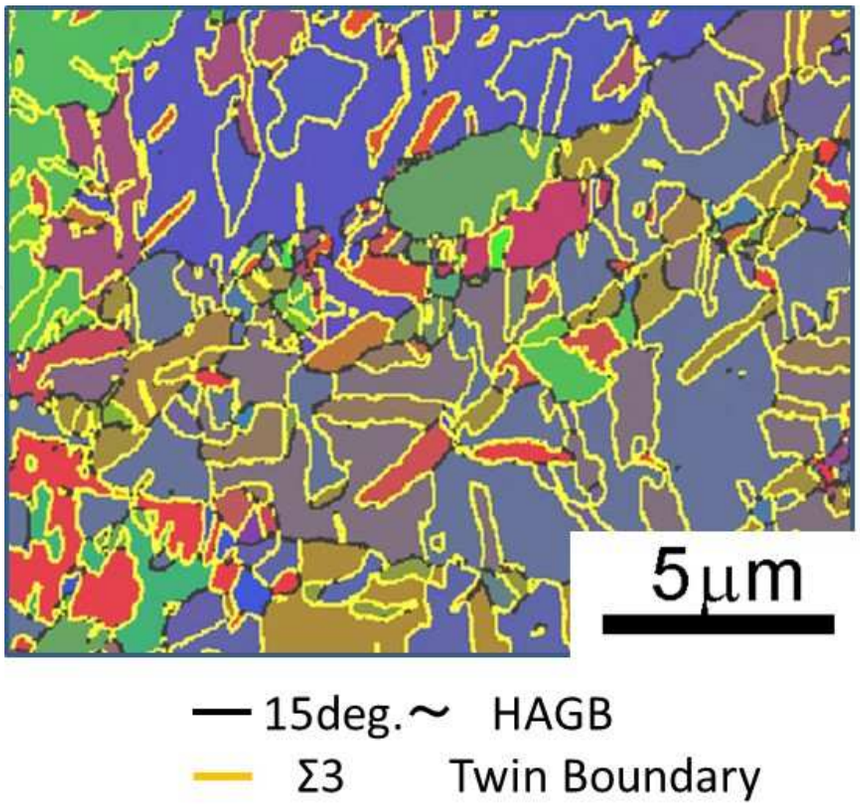

Figure 23. Orientation maps obtained from EP-SCE Cu after two months of storage. Grain boundaries of HAGB and twin boundaries are overlaid in black and yellow lines.

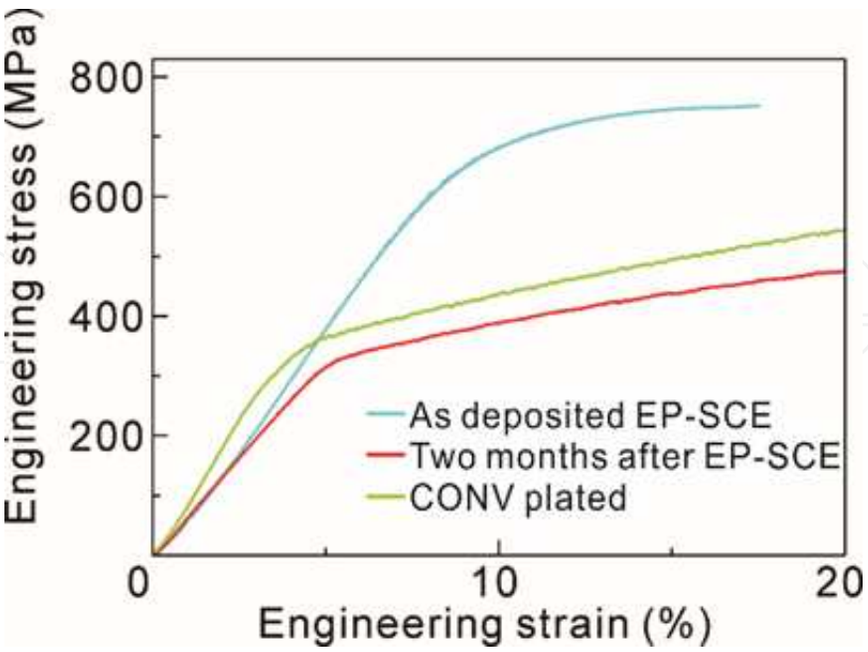

Figure 24. Engineering stress-strain curves in micro-compressions of pillars fabricated from as deposited EP-SCE copper film two months after deposition of EP-SCE copper film and CONV copper film.

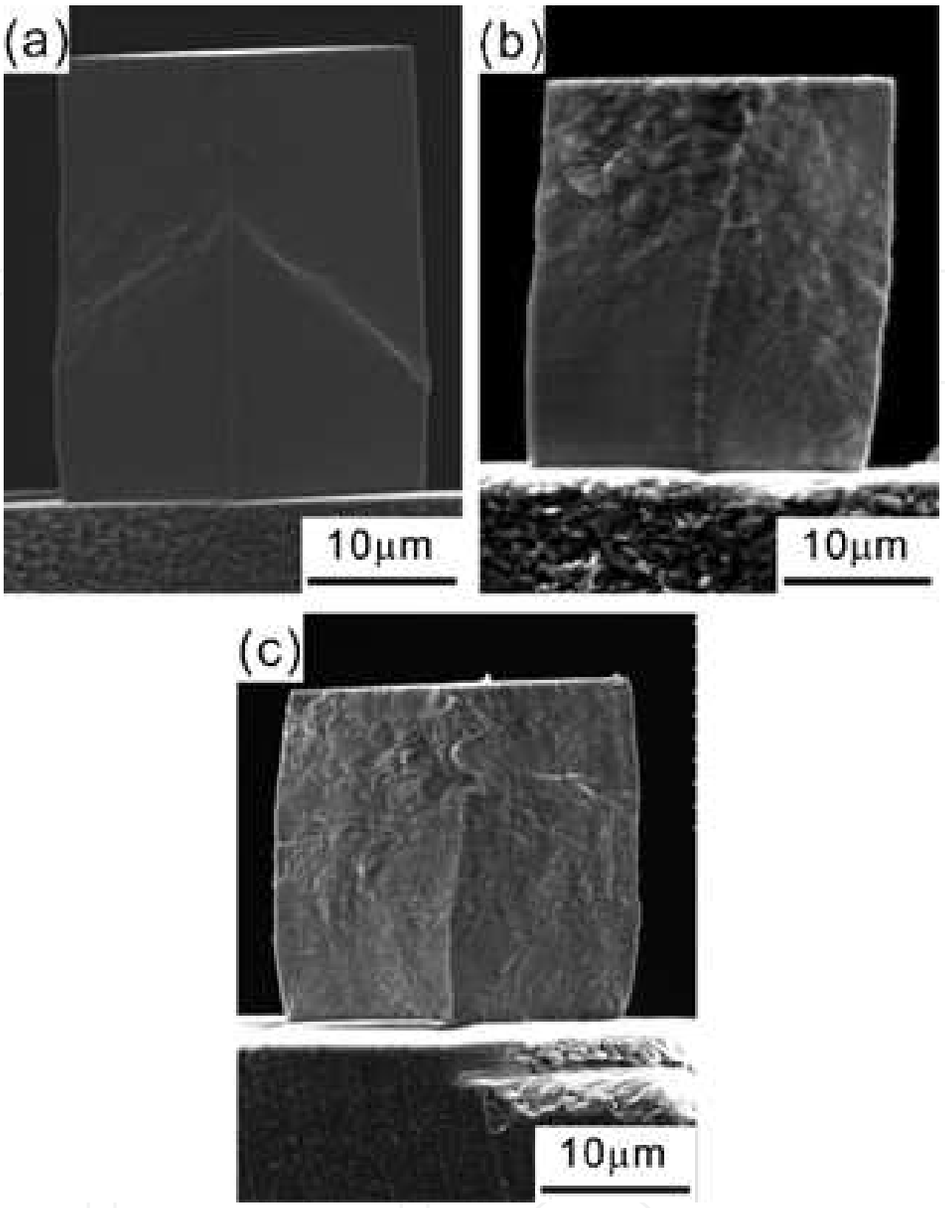

Figure 25. SEM images of post-deformed copper pillar of (a) as-deposited EP-SCE, (b) two months after EP-SCE, and (c) CONV.

Besides limited work hardening, yield stress was increased in the as-deposited EP-SCE pillar compared to self-annealed EP-SCE and CONV pillar. The main reason of strengthening is considered to be grain refinement strengthening. It is widely accepted that grain refinement strengthening is explained as a shortage of dislocation pile-up length due to the decreased distance between grain boundaries. This strengthening contribution was formulated by Hall and Petch and is known as Hall-Petch relationship [67, 68]:

$$\sigma = \sigma_0 + kd^{-\frac{1}{2}}$$

http://dx.doi.org/10.5772/61267

where σ, σ_0, and k are yield strength, friction stress, and the constant for the material, respectively. We calculated the increase in yield strength with decreased grain size from 1.0 to 0.1 μm using the equation. When we refer constant k ($MPa \cdot m^{0.5}$) as 0.14 in previous report on copper [70], the calculated increase in strength was about 300 MPa. This is in good agreement with experimental results of this study. Hence, Cu pillar of as-deposited EP-SCE can be explained only by grain refinement of EP-SCE. Considering the results of GDOES, grain boundary strengthening should be the main factor contributing to the increase of mechanical strength.

4. Conclusions

This chapter describes recent progress in electroplating of micro/nano structures and the evaluation of mechanical properties by micro-testing technique in our group.

Nanocrystalline metals were successfully fabricated using electrodepositon with supercritical CO_2 emulsion. Bouncing micelles desorb hydrogen bubbles and accelerate nucleation by hindering grain growth results in nanocrystalline deposition without defects. Very high strength found in nickel nanocrystals are corresponded to the co-deposited carbon from CO_2. Micro-compression test demonstrated the feasibility for MEMS devices owing to the high strength of nickel. Follow-up micro-testing are also reviewed in this chapter.

Columnar structures of CONV Ni had shown anisotropic mechanical property in micro-cantilever bending. Geometrics of the grains alter the movement of dislocations, resulting in direction-dependent strength of electrodeposited nickel.

Micro-compressions in Cu and Ni revealed size-dependent strength. Materials with S/G ratio smaller than 25 may involve large deviation in mechanical strength. Although in nanocrystalline metals with large S/G ratio tested, increasing strength with decreasing sample size was observed in nickel. This may have corresponded to the CGBS involved in plastic deformation, but further work is needed to explain the detailed mechanisms.

Author details

Takashi Nagoshi[1,2*], Tso-Fu Mark Chang[1] and Masato Sone[1]

*Address all correspondence to: nagoshi-t@aist.go.jp

1 Precision & Intelligence Laboratory, Tokyo Institute of Technology, 4259 Nagatsuta, Midori-ku, Yokohama, Japan

2 National Institute of Advanced Industrial Science and Technology, Tsukuba, Japan

References

[1] Y. Sun, T. Miyasato, J.K. Wigmore, N. Sonoda, Y. Watari, J. Appl. Phys., 2 (1997) 2334.

[2] T. Yoshida, T. Tani, H. Nishimura, K. Akashi, Characterization of a Hybrid Plasma and Its Application to a Chemical Synthesis, J. Appl. Phys., 54 (1983) 640.

[3] M. Gad-el-Hak, The MEMS Handbook; CRC, Taylor & Francis: Boca Raton, Fla., 2006.

[4] J.W. Schultze, A. Bressel, Principles of electrochemical micro- and nano-system technologies, Electrochim. Acta, 47 (2001) 3.

[5] W.L. Tsai, P.C. Hsu, Y. Hwu, C.H. Chen, L.W. Chang, J.H. Je, M.H. Lin, A. Groso, G. Margaritondo, Electrochemistry: Building on bubbles in metal electrodeposition, Nature, 417 (2002) 139.

[6] H. Yoshida, M. Sone, H. Wakabayashi, H. Yan, K. Abe, X.T. Tao, A. Mizushima, S. Ichihara, S. Miyata, New electroplating method of nickel in emulsion of supercritical carbon dioxide and electrolyte solution to enhance uniformity and hardness of plated film, Thin Solid Films, 446 (2004) 194.

[7] H. Yan, M. Sone, N. Sato, S. Ichihara, S. Miyata, The effects of dense carbon dioxide on nickel plating using emulsion of carbon dioxide in electroplating solution, Surf. Coat. Tech., 182 (2004) 329.

[8] H.Yoshida, M.Sone, A.Mizushima, H. An, H.Wakabayashi, K.Abe, X.T.Tao, S.Ichihara, S.Miyata, Application of emulsion of dense carbon dioxide in electroplating solution with nonionic surfactants for nickel electroplating, Surf. Coat. Tech., 173 (2003) 285.

[9] T.F.M Chang, M. Sone, A. Shibata, C. Ishiyama, Y. Higo, Bright nickel deposited by supercritical carbon dioxide emulsion using additive-free Watts bath, Electrochim. Acta, 55 (2010) 6469.

[10] N. Shinoda, T. Shimizu, T.F.M. Chang, A. Shibata, M. Sone, Filling of nanoscale holes with high aspect ratio by Cu electroplating using suspension of supercritical carbon dioxide in electrolyte with Cu particles, Microelectron. Eng., 97C (2012) 126.

[11] T. Shimizu, Y. Ishimoto, T.F.M. Chang, H. Kinashi, T. Nagoshi, T. Sato, M. Sone, Cu wiring into nano-scale holes by electrodeposition in supercritical carbon dioxide emulsified electrolyte with a continuous flow reaction system, J. Supercrit. Fluids, 60 (2014) 60.

[12] A. Shibata, H. Noda, M. Sone, Y. Higo, Microstructural development of an electrodeposited Ni layer, Thin Sol. Film, 518 (2010) 5153.

[13] T. Nagoshi, T.F.M. Chang, T. Sato, M. Sone, Mechanical properties of nickel fabricated by electroplating with supercritical CO2 emulsion evaluated by micro-compression test using non-tapered micro-sized pillar, Microelectron. Eng., 110 (2013) 270.

[14] H. Kinashi, T. Nagoshi, T.F.M. Chang, T. Sato, M. Sone, Mechanical properties of Cu electroplated in supercritical CO2 emulsion evaluated by micro-compression test, Microelectron. Eng., 121 (2014) 83.

[15] M. Tanabe, T.F.M. Chang, T. Nagoshi, S.T. Chung, W.T. Tsai, H. Hosoda, T. Sato, M. Sone, Mechanical properties of Sn electrodeposited in supercritical CO2 emulsions using micro-compression test, Microelectron. Eng., 141 (2015) 219.

[16] J.R. Greer, W.D. Nix, Nanoscale gold pillars strengthened through dislocation starvation, Acta Mater., 53 (2005) 1821.

[17] G. Dehm, T. Wagner, T.J. Balk, E. Arzt, B.J. Inkson, Plasticity and interfacial dislocation mechanisms in epitaxial and polycrystalline Al films constrained by substrates, J. Mater. Sci. Tech., 18 (2002)113.

[18] P.A. Gruber, J. Bohm, F. Onuseit, A. Wanner, R. Spolenak, E. Arzt, Size effects on yield strength and strain hardening for ultra-thin Cu films with and without passivation: A study by synchrotron and bulge test techniques, Acta Mater., 56 (2008) 2318.

[19] M.A. Haque, M.T.A. Saif, A Review of MEMS-Based Microscale and Nanoscale Tensile and Bending Testing, Experimental Mech., 43 (2003) 248.

[20] C.P. Frick, B.G. Clark, S. Orso, A.S. Schneider, E. Arzt, Size effect on strength and strain hardening of small-scale [111] nickel compression pillars, Mater. Sci. Eng. A, 489 (2008) 319.

[21] D.M. Dimiduk, M.D. Uchic, T.A. Parthasarathy, Size-affected single-slip behavior of pure nickel microcrystals, Acta Mater., 53 (2005) 4065.

[22] Z.M. Shan, R. Mishra R, S.A. Syed, O.L. Warren, A.M. Minor. Mechanical annealing and source-limited deformation in submicron diameter Ni crystals. Nature Mater., 7 (2008) 115

[23] J.R. Greer, W.C. Oliver, W.D. Nix. Size dependence of mechanical properties of gold at the micron scale in the absence of strain gradients, Acta Mater., 53 (2005) 1821.

[24] C.M. Byer, B. Li, B. Cao, K.T. Ramesh. Microcompression of single-crystal magnesium, Scripta Mater. 62 (2010) 536.

[25] J.Y. Kim, J.R. Greer. Tensile and compressive behavior of gold and molybdenum single crystals at the nano-scale, Acta Mater., 57 (2009) 5245.

[26] S. Cheng, X.L. Wang, H. Choo, P.K. Liaw. Global melting of Zr57Ti5Ni8Cu20Al10 bulk metallic glass under micro-compression, Appl. Phys. Lett., 91 (2007) 201917.

[27] B.E. Schuster, Q. Wei, M.H. Ervin, S.O. Hruszkewycz, M.K. Miller, T.C. Hufnagel, K.T. Ramesh. Bulk and microscale compressive properties of a Pd-based metallic glass, Scripta Mater., 57 (2007) 517.

[28] Y.H. Lai, C.J. Lee, Y.T. Cheng, H.S. Chou, H.M. Chen, X.H. Du, C.I. Chang, J.C. Huang, S.R. Jian, J.S.C. Jang, T.G. Nieh, Bulk and microscale compressive behavior of a Zr-based metallic grass, Scripta Mater., 58 (2008) 890.

[29] F.F. Wu, Z.F. Zhang, S.X. Mao. Size-dependent shear fracture and global tensile plasticity of metallic glasses. Acta Mater., 57 (2009) 257.

[30] A. Rinaldi, P. Peralta, C. Friesen, K. Sieradzki, Sample size-effects in the yield behavior of nanocrystalline Ni, Acta Mater., 56 (2008) 511.

[31] D. Jang, J. R. Greer, Size-induced weakening and grain boundary-assisted deformation in 60 nm grained Ni nanopillars, Scripta Mater., 64 (2011) 77-80.

[32] F.J. Humphreys, M. Hartherly, Recrystallization and Related Annealing Phenomena, second ed. Elsevier, Amsterdam, 2004.

[33] S. Nakahara, Growth twins and development of polycrystallinity in electrodeposits J. Cryst. Growth 55 (1981) 281.

[34] A. Bastos, S. Zaefferer, D. Raabe, C. Schuh, Characterization of the microstructure and texture of nanostructured electrodeposited NiCo using electron backscatter diffraction (EBSD), Acta Mater., 54 (2006) 2451.

[35] E. Shinada, T. Nagoshi, T.F.M. Chang, M. Sone, Crystallographic study on self-annealing of electroplated copper at room temperature, Mater. Sci. Semicon., 16 (2013) 633.

[36] K. Fujiwara, K. Maeda, N. Usami, G. Sazaki, Y. Nose, K. Nakajima, Formation mechanism of parallel twins related to Si-facetted dendrite growth, Scr. Mater., 57 (2007) 81.

[37] K. Fujiwara, K. Maeda, N. Usami, G. Sazaki, Y. Nose, A. Nomura, T. Shishido, K. Nakajima, In situ observation of Si faceted dendrite growth from low-degree-of-undercooling melts, Acta Mater., 56 (2008) 2663.

[38] K. Fujiwara, K. Maeda, N. Usami, K. Nakajima, Growth Mechanism of Si-Faceted Dendrites, Phys. Rev. Lett., 101 (2008) 055503.

[39] C. Motz, T. Schöberl, R. Pippan, Mechanical properties of micro-sized copper bending beams machined by the focused ion beam technique, Acta Mater., 53 (2005) 4269.

[40] A. Shibata, T. Nagoshi, M. Sone, S. Morito, Y. Higo, Evaluation of the block boundary and sub-block boundary strengths of ferrous lath martensite using a microbending test, Mater. Sci. Eng. A, 527 (2010) 7538.

[41] F. Iqbal, J. Ast, M. Göken, K. Durst, In-situ micro-cantilever tests to study fracture properties of NiAl single crystals, Acta Mater., 60 (2012) 1193.

[42] H. Imamura, T. Nagoshi, A. Yoshida, T.F.M. Chang, S. Onaka, M. Sone, Evaluation of anisotropic structure in electrodeposited Ni film using micro-sized cantilever, Microelectron. Eng., 100 (2012) 25.

[43] T.F.M. Chang, M. Sone, Function and mechanism of supercritical carbon dioxide emulsified electrolyte in nickel electroplating reaction, Surface and Coating Technology, 205 (2011) 3890-3899.

[44] S.T. Chung, and W.T. Tsai, Nanocrystalline Ni-C electrodeposits prepared in electrolytes containing supercritical carbon dioxide, J. Electrochim. Soc., 156 (2009) D457.

[45] N. Yamachika, Y. Musha, J. Sasano, K. Senda, M. Kato, Y. Okinaka, T. Osaka, Electrodeposition of amorphous Au-Ni alloy film, Electrochimica Acta, 53, (2008) 4520.

[46] Y. Hori, K. Kikuchi, S. Suzuki, Production of CO and CH4 in electrochemical reduction of CO2 at metal electrodes in aqueous hydrogencarbonate solution, Chemistry Letters, 11 (1985) 1695.

[47] J.W. Cahn, The impurity-drag effect in grain boundary motion, Acta Metall., 10 (1962) 789.

[48] A.J. Detor, C.A. Schuh, Tailoring and patterning the grain size of nanocrystalline alloys, Acta Mater., 55 (2007) 371.

[49] F. Liu, R. Kirchheim, Nano-scale grain growth inhibited by reducing grain boundary energy through solute segregation, J. Cryst. Growth, 264 (2004) 385

[50] L.G. Wang, C.Y. Wang, First-principles calculations of energies of impurities and doping effects at grain boundaries in nickel Mater. Sci. Eng. A, 234 (1997) 521.

[51] R.L. Fleischer, Solution hardening, Acta Metall., 9 (1961) 996.

[52] C.A. Schuh, T.G. Nieh, T. Yamasaki, Hall-Petch Breakdown Manifested in Abrasive. Wear Resistance of Nanocrystalline Nickel, Scripta Mater., 46(2002) 735.

[53] F. Ebrahimi, G.R. Bourne, M.S. Kelly and T.E. Matthews, Mechanical properties of nanocrystalline nickel produced by electrodeposition, Nanostruct. Mater., 11 (1999) 343.

[54] G.D. Hughes, S.D. Smith, C.S. Pande, H.R. Johnson, R.W. Armstrong, Hall-Petch strengthening for the microhardness of twelve nanometer grain diameter electrodeposited nickel, Scripta Metall., 20 (1986) 93.

[55] C.A. Schuh, T.G. Nieh, H. Iwasaki, The effect of solid solution W additions on the mechanical properties of nanocrystalline Ni, Acta Mater., 51 (2003) 431.

[56] D. Tabor, The Hardness of Metals, Oxford University Press, London, 1951.

[57] W.M. Yin, S.H. Whang, R.A. Mirshams, The Fracture Toughness of Thin Sheet Nanocrystalline Pure and Carbon Doped Nickel, Acta Mater., 53 (2005) 383.

[58] Y. Kihara, T. Nagoshi, T.F.M. Chang, H. Hosoda, T. Sato, M. Sone, Tensile behavior of micro-sized specimen fabricated from nanocrystalline nickel film, Microelectron. Eng., 141 (2015) 17.

[59] T. Nagoshi, T.F.M. Chang, T. Sato, M. Sone, Sample size effect of electrodeposited nickel with sub-10 nm grain size, Mater. Lett., 117 (2014) 256.

[60] M.G. Zelin, A. K. Mukherjee, Acta Metall. Mater., 43 (1995) 2359.

[61] M. Stangl, M.Lipták, A.Fletcher, J.Acker, J.Thomas, H.Wendrock, S.Oswald, K.Wetzig, Influence of initial microstructure and impurities on Cu room-temperature recrystallization (self-annealing), Microelectron. Eng., 85 (2008) 534.

[62] C. Lingk and M. E. Gross, Recrystallization kinetics of electroplated Cu in damascene trenches at room temperature, J. Appl. Phys., 84 (1998) 5547.

[63] M. E. Gross, K. Takahashi, C. Lingk, T. Ritzdorf, and K. Gibbons: Advanced Metallization Conf. 1998, ed. G.S. Sandhu, H. Koerner, M. Murakami, Y. Yasuda, N. Kobayashi, Pittsburgh, PA: Materials Research Society, (1999) 51.

[64] D.A. Porter, K.E. Easterling, M.Y. Sherif, Phase Transformations in Metals and Alloys, Third ed., CRC Press, Boca Raton, 2014.

[65] R.W. Armstrong, On size effects in polycrystal plasticity, J. Mech. Phys. Solids, 9 (1961) 196.

[66] M. Mutoh, T. Nagoshi, T.F.M.Chang, T. Sato, M. Sone, Micro-compression test using non-tapered micro-pillar of electrodeposited Cu, Microelectron. Eng., 111 (2013) 118.

[67] E.O. Hall, The Deformation and Ageing of Mild Steel: III Discussion of Results, Proc. Phys. Soc. London B, 64 (1951) 747.

[68] N.J. Petch, The Cleavage Strength of Polycrystals, J. Iron Steel Inst., 174 (1653) 25.

[69] W.L. Chan, M.W. Fu, J. Lu, J.G. Liu, Modeling of grain size effect on micro deformation behavior in micro-forming of pure copper, Mater. Sci. Eng. A, 527 (2010) 6638.

[70] G.D. Hughes, S.D. Smith, C.S. Pande, H.R. Johnson, R.W. Armstrong, Hall-Petch strengthening for the microhardness of twelve nanometer grain diameter electrodeposited nickel, Scripta Metall., 20 (1986) 93.